


# NuSTAR spectral analysis of three Seyfert galaxies: NGC 3227, NGC 5548, and MR 2251–178

I. Pal<sup>1,2</sup> , C. S. Stalin<sup>1</sup>, L. Mallick<sup>4,1</sup>, and P. Rani<sup>3</sup>

<sup>1</sup> Indian Institute of Astrophysics, Bangalore, India  
e-mail: [indrani.pal@iiap.res.in](mailto:indrani.pal@iiap.res.in)

<sup>2</sup> Pondicherry University, R.V. Nagar, Kalapet, 605014 Puducherry, India

<sup>3</sup> Inter University Centre for Astronomy and Astrophysics, Pune, India

<sup>4</sup> Cahill Center for Astronomy and Astrophysics, California Institute of Technology, Pasadena, CA 91125, USA

Received 7 October 2021 / Accepted 28 February 2022

## ABSTRACT

**Context.** The observed nuclear X-ray emission in the radio-quiet category of active galactic nuclei (AGN) is believed to be from a compact region, the corona, which is situated in the vicinity of central supermassive black holes. The shape of the X-ray continuum depends on, among other factors, the temperature of the corona ( $kT_e$ ). The launch of the Nuclear Spectroscopic Telescope Array (*NuSTAR*) has led to the determination of the high energy cutoff ( $E_{\text{cut}}$ ), and thereby  $kT_e$ , in many AGN. In a handful of sources, multiple observations with *NuSTAR* have also revealed changes in  $E_{\text{cut}}$ .

**Aims.** In this work we aimed to investigate the variation in  $kT_e$  in three AGN, namely NGC 3227, NGC 5548, and MR 2251–178, using more than one epoch of data on a source from *NuSTAR*.

**Methods.** We carried out a spectral analysis of multiple epochs of data acquired using *NuSTAR* on the three sources, including a few new observations that had not yet been published. By fitting a Comptonization model to the data, we determined the temperature of the corona and investigated changes in  $kT_e$ , if there were any, in these sources.

**Results.** In NGC 3227, we found evidence for variation in  $kT_e$ . We found no correlation of  $kT_e$ , photon index ( $\Gamma$ ), reflection fraction ( $R$ ), or optical depth ( $\tau$ ) with flux, while  $\tau$  is found to anti-correlate with  $kT_e$ . This could be due to more than one physical process at work in the source causing the change in  $kT_e$ . Conclusive evidence for the variation in  $kT_e$  is not found in MR 2251–178 or NGC 5548.

**Key words.** galaxies: active – galaxies: Seyfert – X-rays: galaxies

## 1. Introduction

Active galactic nuclei (AGN) are amongst the most luminous objects ( $L = 10^{42}$ – $10^{46}$  erg s<sup>-1</sup>; Fabian 1999) in the Universe that emit radiation over a wide range of wavelengths. They are believed to be powered by the accretion of matter onto supermassive black holes (SMBHs;  $10^5$ – $10^9 M_\odot$ ) situated at the centres of galaxies (Rees 1984; Dewangan et al. 2008). The SMBH is generally supposed to be surrounded by an optically thick and geometrically thin accretion disk (Shakura & Sunyaev 1973). The observed X-ray emission from the nuclear region of the radio-quiet category of AGN is believed to be produced by an inverse Compton process; this process is caused by the interaction of the seed ultraviolet (UV) photons from the accretion disk with the thermal electrons in a hot ( $\sim 10^8$ – $10^9$  K) region called the corona, which is situated close to the accretion disk (Haardt & Maraschi 1991; Haardt et al. 1994). This X-ray continuum gets reprocessed in the accretion disk, giving rise to the reflection hump at around 15–30 keV as well as the broad FeK $\alpha$  line at 6.4 keV (George & Fabian 1991; Matt et al. 1993). Soft excess between 0.1–2 keV is ubiquitously observed in Type I AGN (Magdziarz et al. 1998; Fabian et al. 2002; Crummy et al. 2006; Bianchi et al. 2009; Gliozzi & Williams 2020), although the physical origin of this component remains highly debated (García et al. 2019; Xu et al. 2021). Different analyses have shown that a two-temperature Comptonization

process agrees well with such a component from either an observational (e.g., Jin et al. 2012; Porquet et al. 2018; Petrucci et al. 2018; Middei et al. 2020; Matzeu et al. 2020) or theoretical (e.g., Rózańska et al. 2015; Petrucci et al. 2020; Ballantyne 2020; Ballantyne & Xiang 2020) point of view. Analysis of these spectral features (reflection, FeK $\alpha$  line, soft excess) will help in providing strong constraints on the nature of the X-ray emitting region. From X-ray reverberation studies (Fabian et al. 2009; Zoghbi et al. 2012), the AGN corona is believed to be a compact region situated above the accretion disk, typically within 3–10 $R_G$ ; here,  $R_G$  is the gravitational radius, defined as  $R_G = GM_{\text{BH}}/c^2$ , where  $M_{\text{BH}}$  is the SMBH mass and  $G$  is the gravitational constant. However, there has been a great deal of debate concerning the geometry of the corona. The lamp post is one such possibility, but other models also exist (e.g., Haardt et al. 1994; Done et al. 2012; Petrucci et al. 2013). Also, rapid X-ray flux variability studies (McHardy et al. 2005), the observed small timescales of X-ray eclipses (Risaliti et al. 2005, 2011), and microlensing studies (Chartas et al. 2009) all point to the X-ray corona having a small size, 5–10 $R_G$ .

The observed shape of the X-ray continuum can be described by a power law with an exponential cutoff ( $E_{\text{cut}}$ ), and the spectral shape depends on the optical depth ( $\tau$ ), the temperature of the coronal plasma ( $kT_e$ ), the seed photon temperature, and the viewing angle. From a study of the Seyfert galaxy NGC 5548, Petrucci et al. (2000) showed the existence of an approximate

relation between  $E_{\text{cut}}$  and  $kT_e$  as  $E_{\text{cut}} = 2-3kT_e$ . From an analysis of a sample of Seyfert galaxies, [Petrucci et al. \(2001\)](#) found  $E_{\text{cut}} \approx 2kT_e$  for an optically thin corona with  $\tau < 1$  and  $E_{\text{cut}} \approx 3kT_e$  for an optically thick corona with  $\tau > 1$ . However, by fitting Comptonized spectra simulated using a range of  $\tau$  and  $kT_e$  with a power law with an exponential cutoff model, [Middei et al. \(2019\)](#) showed that the commonly adopted relation of  $E_{\text{cut}} = 2-3kT_e$  is not valid for all values of  $\tau$  and  $kT_e$ ; it is only valid for low values of  $\tau$  and  $kT_e$ .

Observations from high energy X-ray missions such as CGRO ([Zdziarski et al. 2000](#); [Johnson et al. 1997](#)), *BeppoSAX* ([Nicastro et al. 2000](#); [Dadina 2007](#)), INTEGRAL ([Malizia et al. 2014](#); [Lubiński et al. 2010, 2016](#); [Ricci et al. 2011](#)), *Swift*-BAT ([Vasudevan et al. 2013b](#); [Ricci et al. 2017](#)), and Suzaku ([Tazaki et al. 2011](#)) have shown that the coronae in Seyfert galaxies have a wide range of temperatures, with  $E_{\text{cut}}$  ranging from 50–500 keV. However, observations from those missions are limited to bright and nearby sources. Thus, it is very clear that it took a great deal of effort to measure  $E_{\text{cut}}$  in the X-ray spectra of several AGN. However, a major transformation in the study of the Comptonization spectrum of AGN – determining  $E_{\text{cut}}$  from an epoch of observation – occurred after the launch of the Nuclear Spectroscopic Telescope Array (*NuSTAR*; [Harrison et al. 2013](#)) in the year 2012, owing to its broad spectral coverage of 3–79 keV and its high sensitivity beyond 10 keV. Since the launch of *NuSTAR*,  $E_{\text{cut}}$  values have been obtained for many AGN ([Fabian et al. 2017](#); [Tortosa et al. 2018](#); [Rani & Stalin 2018a,b](#); [Rani et al. 2019](#); [Lanzuisi et al. 2019](#); [Baloković et al. 2020](#); [Reeves et al. 2021](#); [Kang et al. 2021](#)). Importantly, in addition to the determination of  $E_{\text{cut}}$  values (and thereby the constraining of  $kT_e$ ), there are also reports of variation in the  $E_{\text{cut}}$  values that point to variations in  $kT_e$  in a few sources.

For example, in seven sources, namely MCG-5-23-16 ([Zoghbi et al. 2017](#)), 3C 382 ([Ballantyne et al. 2014](#)), NGC 4593 ([Ursini et al. 2016](#)), NGC 5548 ([Ursini et al. 2015](#)), Mrk 335 ([Keek & Ballantyne 2016](#)), NGC 3227, and SWIFT J2127.4+5654 ([Kang et al. 2021](#)), variations in the  $E_{\text{cut}}$  values are available in the literature. Recently, from a reanalysis of the *NuSTAR* spectra of five sources using a model-independent approach, [Zhang et al. \(2018\)](#) confirmed the  $E_{\text{cut}}$  variation in three of the five sources, namely 3C 382, NGC 5548, and Mrk 335. Most of these inferences were based on variations in  $E_{\text{cut}}$  obtained from phenomenological model fits to the data. However, to determine changes in  $kT_e$ , it is imperative to fit physical models to the data because, as has recently been learned, the relation  $E_{\text{cut}} = 2-3kT_e$  does not always hold true ([Middei et al. 2019](#)). Therefore, it is imperative to fit physical model fits to the observed spectra to get  $kT_e$ . Though  $E_{\text{cut}}$  is known to vary, we do not yet know the causes for its variation. Despite that, it is important to increase the number of sources that show variation in the temperature of the corona. This is now achievable owing to the multiple epochs of observation available for a large number of AGN in the *NuSTAR* archives<sup>1</sup>. The primary motivation here is, therefore, to increase the number of known AGN that show variation in  $kT_e$ . We are in the process of a careful and systematic investigation of  $kT_e$  variation in a large number of AGN. Here, we present the results from the multi-epoch spectral analysis of three AGN, namely NGC 3227, NGC 5548, and MR 2251–178. This paper also includes a few new observations that had not been published.

NGC 3227, at a redshift of  $z = 0.004$  and powered by a black hole of mass  $4.79 \times 10^6 M_{\odot}$  ([Bentz & Katz 2015](#)), has been extensively studied in the X-ray band. Signatures of warm absorbers are evident in this source from observations with ASCA ([Netzer et al. 1994](#); [George et al. 1998](#)), ROSAT ([Komossa & Fink 1997](#)), and *XMM-Newton* ([Markowitz et al. 2009](#)). In the *XMM-Newton* observations, the FeK $\alpha$  line was evident ([Markowitz et al. 2009](#)). It has also recently been studied for flux variations by [Lobban et al. \(2020\)](#), who combined *XMM-Newton* and *NuSTAR* observations. It has complex absorption features, which are also variable ([Turner et al. 2018](#)). Recently, [Mehdipour et al. \(2021\)](#) reported the broadband spectral modelling of the source using multi-wavelength data from *XMM-Newton*, *NuSTAR*, and the *Hubble* Space Telescope. NGC 5548 is a galaxy located at  $z = 0.017$  with a black hole of mass of  $5.0 \times 10^7 M_{\odot}$  ([Bentz & Katz 2015](#)). It has been extensively studied in the X-ray band via data from various satellites and has also been found to be strongly absorbed in soft X-rays ([Cappi et al. 2016](#); [Ursini et al. 2015](#); [Mehdipour et al. 2015](#); [Kaastra et al. 2014](#)). MR 2251–178, with a black hole mass of  $2.0 \times 10^8 M_{\odot}$  ([Wang et al. 2009](#)), was first discovered thanks to its strong X-ray emission ([Ricker et al. 1978](#)) and has been found to be a low redshift AGN at  $z = 0.06$  ([Bergeron et al. 1983](#)). From Very Large Array observations, [Macchetto et al. \(1990\)](#) found the source to show weak radio emission with an elongated morphology, resembling a FRI (Fanaroff-Riley Class I) source. Details of the observations and reduction of the data are presented in Sect. 2, analysis is presented in Sect. 3, and results and a discussion are presented in Sect. 4, followed by a summary in the final section.

## 2. Observations and data reduction

We reduced *NuSTAR* data in the 3–79 keV band using the standard *NuSTAR* data reduction software NuSTARDAS<sup>2</sup>, which is distributed by HEASARC within HEASoft v6.29. Considering the passage of the satellite through the South Atlantic Anomaly (SAA), we selected SAACALC ‘2’ and SAAMODE ‘optimized’ and excluded the tentacle region. The calibrated, cleaned, and screened event files were generated by running the *nupipeline* task using CALDB release 20210701. To extract the source counts, we chose a circular region of radius 60 arcsec centred on the source. Similarly, to extract the background counts, we selected a circular region of the same radius away from the source on the same chip to avoid contamination from source photons. We then used the *nuproducts* task to generate energy spectra, response matrix files, and auxiliary response files for both of the hard X-ray detectors housed inside the corresponding focal plane modules, FPMA and FPMB. For spectral analysis, using XSPEC version 12.12.0 ([Arnaud 1996](#)), we fitted the background subtracted spectra from FPMA and FPMB simultaneously (without combining them), allowing the cross-normalization factor to vary freely during spectral fits. The spectra were binned to have a S/N greater than 5 in each spectral channel using the *NuSTAR*-specific Python script *snrgppha*<sup>3</sup>. To get an estimate of the model parameters that best describe the observed data, we used the chi-squared ( $\chi^2$ ) statistics, and for calculating the errors in the model parameters we used the  $\chi^2 = 2.71$  criterion (i.e. 90 per cent confidence range) in XSPEC.

<sup>2</sup> [http://heasarc.gsfc.nasa.gov/docs/nustar/analysis/nustar\\_swguide.pdf](http://heasarc.gsfc.nasa.gov/docs/nustar/analysis/nustar_swguide.pdf)

<sup>3</sup> <https://sites.astro.caltech.edu/~mislavb/>

<sup>1</sup> <https://heasarc.gsfc.nasa.gov/cgi-bin/W3Browse/w3browse.pl>

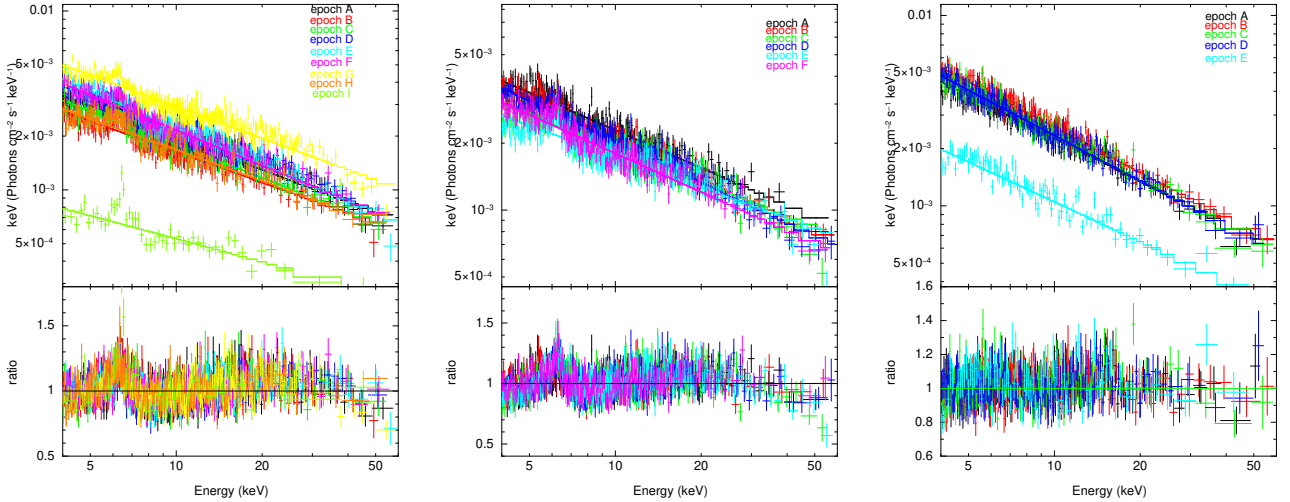


**Fig. 1.** Unfolded spectra of the nine observations for NGC 3227 (*left*), six observations for NGC 5548 (*middle*), and five observations for MR 2251–178 (*right*) fitted with a simple power law. *Bottom panels:* ratio of the observed spectra to the model. For clarity, we used only FPMA data. The spectra are re-binned for visualization purposes only.

### 3. Analysis of the data

For a few epochs of the sources studied in this work, we do have observations in the soft band from telescopes such as *XMM-Newton* for NGC 3227, *XMM-Newton* and *Chandra* for NGC 5548, and *XMM-Newton* for MR 2251–178. However, for this work we decided to use only *NuSTAR* data as (a) the good sensitivity of *NuSTAR* over the 3–79 keV energy band captures all the key reflection features of an AGN spectrum and, as the main goal of this work is to model the high energy rollover of the Comptonized spectra, we did not want the absorption in the soft band affecting our analysis in the determination of  $kT_e$ , and (b) observations in the soft band are not available simultaneous to the *NuSTAR* observations for all the epochs and for all the sources. However, we note here that the inclusion of soft X-ray data in the fitting might have an effect on the photon index ( $\Gamma$ ) obtained from using the *NuSTAR* data alone. The simplest approach to constraining  $kT_e$  (which is the aim of this work) is the use of only *NuSTAR* data, but to better constrain the other physical characteristics of the sources, broadband spectral analysis that includes data from the UV band to the hard X-ray band is more appropriate. While analysing only *NuSTAR* data, we ignored the 3–4 keV band to limit the effect of absorption, if any, and did not consider data in the energy range beyond 60 keV due to a lack of source photons. Thus, we carried out spectral fits to the *NuSTAR* data in the 4–60 keV energy band for all the observation IDs (ObsIDs) except for epoch I of NGC 3227, epoch F of NGC 5548, and epoch E of MR 2251–178. Due to the unavailability of photons beyond 50 keV, we restricted the spectral fit in the 4–50 keV energy band to the epoch I and epoch E spectra of NGC 3227 and MR 2251–178, respectively. Similarly, for the epoch F spectrum of NGC 5548, we used the FPMA/FPMB data in the 4–55 keV range (see Fig. 1).

#### 3.1. Phenomenological spectral fits

For our spectral fits, to model the line of sight galactic absorption, the value of the neutral hydrogen column densities ( $N_H$ ) for all the sources were frozen to the values obtained from Willingale et al. (2013). These  $N_H$  values are given in Table 1. Similarly, the redshifts of the sources were frozen

to the corresponding values given in Table 1. Also, we used the solar abundances from Wilms et al. (2000) and the photoelectric cross-sections from Verner et al. (1996). For models that require an inclination angle ( $i$ ), we used  $i=50^\circ$  for NGC 3227 (Schmitt et al. 1997; Alonso-Herrero et al. 2019; Middleton et al. 2016),  $i=30^\circ$  for NGC 5548 (Ursini et al. 2015), and  $i=60^\circ$  (i.e. the default value) for MR 2251–178.

##### 3.1.1. Absorbed power law

Firstly, to understand the continuum emission in our sample of sources, we fitted the observed X-ray spectra with the baseline phenomenological absorbed power law model that has the following form in XSPEC:

$$\text{const} * TBabs(zpo). \quad (1)$$

The first component of this model is the constant used to calibrate the two focal plane modules of *NuSTAR*. The second component,  $TBabs$  (Wilms et al. 2000), was used to model the line of sight galactic absorption. The parameters that were kept free are  $\Gamma$  and the normalization (i.e. photons in  $\text{keV}^{-1} \text{cm}^{-2} \text{s}^{-1}$ ). We found evidence of intrinsic absorption present in the lower energy end for all the epochs in NGC 5548, epochs G, H, and I in NGC 3227, and epoch E in MR 2251–178. We therefore included a  $zTBabs$  component with the absorbed power law model to fit their spectra, and the model appears as

$$\text{const} * TBabs * zTBabs(zpo) \quad (2)$$

in XSPEC. For all epochs in NGC 5548, two epochs in NGC 3227, and one epoch of MR 2251–178, the non-inclusion of  $zTBabs$  returned a poor fit, with  $\chi^2/\text{d.o.f.}$  larger than 1.2. Inclusion of  $zTBabs$  with  $N_H(zTBabs)$  kept free improved the fit, with  $\chi^2/\text{d.o.f.}$  close to unity.

From the residual spectra obtained from the simple absorbed power law model fit to the observations, we noticed the presence of the fluorescent  $\text{FeK}\alpha$  line in NGC 3227, NGC 5548, and in epoch D spectra of MR 2251–178, but in the other observations of MR 2251–178 the residual spectra do not show a conspicuous  $\text{FeK}\alpha$  line. The spectral fits are shown in Fig. 1 for NGC 3227, NGC 5548, and MR 2251–178. Though this line is common in most of the X-ray spectra of AGN (Mushotzky et al. 1993;



**Table 1.** Details of the sources analysed in this work.

| Name               | $\alpha_{2000}$ | $\delta_{2000}$ | $z$   | $N_{\text{H}}$ | Type  | ObsID              | Epoch       | Date       | Exposure |
|--------------------|-----------------|-----------------|-------|----------------|-------|--------------------|-------------|------------|----------|
| NGC 3227           | 10:23:30.60     | +19:51:56       | 0.004 | 0.021          | Sy1.5 | 60202002002        | A           | 09-11-2016 | 49800    |
|                    |                 |                 |       |                |       | 60202002004        | B           | 25-11-2016 | 42457    |
|                    |                 |                 |       |                |       | 60202002006        | C           | 29-11-2016 | 39685    |
|                    |                 |                 |       |                |       | 60202002008        | D           | 01-12-2016 | 41812    |
|                    |                 |                 |       |                |       | 60202002010        | E           | 05-12-2016 | 40887    |
|                    |                 |                 |       |                |       | 60202002012        | F           | 09-12-2016 | 39277    |
|                    |                 |                 |       |                |       | 60202002014        | G           | 21-01-2017 | 47602    |
|                    |                 |                 |       |                |       | <b>80502609002</b> | H           | 15-11-2019 | 28782    |
|                    |                 |                 |       |                |       | <b>80502609004</b> | I           | 05-12-2019 | 27690    |
|                    |                 |                 |       |                |       | NGC 5548           | 14:17:59.53 | +25:08:12  | 0.017    |
| 60002044003        | B               | 12-07-2013      | 27272 |                |       |                    |             |            |          |
| 60002044005        | C               | 23-07-2013      | 49521 |                |       |                    |             |            |          |
| 60002044006        | D               | 10-09-2013      | 51460 |                |       |                    |             |            |          |
| 60002044008        | E               | 20-12-2013      | 50102 |                |       |                    |             |            |          |
| <b>90701601002</b> | F               | 26-01-2021      | 38719 |                |       |                    |             |            |          |
| MR 2251–178        | 22:54:05.90     | –17:34:55       | 0.064 | 0.027          | Sy1.5 |                    |             |            |          |
|                    |                 |                 |       |                |       | <b>60102025004</b> | B           | 17-06-2015 | 23185    |
|                    |                 |                 |       |                |       | <b>60102025006</b> | C           | 10-11-2015 | 20588    |
|                    |                 |                 |       |                |       | <b>60102025008</b> | D           | 11-12-2015 | 21707    |
|                    |                 |                 |       |                |       | <b>90601637002</b> | E           | 16-12-2020 | 23620    |

**Notes.** Columns are (1) name of the source, (2) right ascension (h:m:s), (3) declination (d:m:s), (4) redshift, (5) galactic hydrogen column density,  $N_{\text{H}}$ , in units of  $10^{22}$  atoms  $\text{cm}^{-2}$  obtained from Willingale et al. (2013), (6) type of the source, (7) observation ID (ObsID), (8) epoch, (9) date of observation, and (10) exposure time in sec. Some of the information, including the right ascension, declination, and  $z$ , are from Véron-Cetty & Véron (2010). The ObsIDs that are analysed for the first time are shown in bold.

Nandra et al. 2007; Della Ceca et al. 2010), there are exceptions (Bhayani & Nandra 2011). The apparent non-detection of a FeK $\alpha$  line in the spectra of MR 2251–178 could be due to a weaker reflection that is a result of a larger viewing angle (Bhayani & Nandra 2011), low signal-to-noise ratio spectra, a very high-ionized accretion disk (Ross & Fabian 1993; Zycki & Czerny 1994), or a combination of all three. However, the presence of a weak FeK $\alpha$  line in epoch D of MR 2251–178 could point to the physical characteristics of MR 2251–178 being different from those of the other two sources. A thorough analysis is needed to know the exact reasons for the absence or weakness of this line, but this issue is beyond the scope of this work; here we are mainly interested in the changes in the temperature of the corona. To model the FeK $\alpha$  line seen in the residual spectra in NGC 3227 and NGC 5548 and in one observation (epoch D) of MR 2251–178, we included a Gaussian component; with this inclusion, the model takes the form  $const*TBabs(zpo + zgauss)$ , and the quality of the fit improved.

After the inclusion of a Gaussian component with the power law in the case of NGC 3227, in all nine epochs the  $\chi^2$  value in the range between 60 and 242 was reduced, for a reduction of 2 d.o.f. In epochs C, D, G, and I, non-inclusion of the Gaussian component resulted in a reduced  $\chi^2$  of more than 1.30. After the inclusion of the Gaussian component, the reduced  $\chi^2$  ranged between 1.04–1.16 in these epochs. For the other epochs, the  $\chi^2$ /d.o.f. was  $>1.1$  before, and it became  $\sim 1.0$  after the line inclusion. For MR2251–178, a Gaussian component was used to fit the FeK $\alpha$  line only in epoch D. Inclusion of the line component led to a change in  $\chi^2$  of 5 for a reduction of 2 d.o.f. This negligible change in  $\chi^2$  over 2 d.o.f. did not improve the fit quality significantly in this case. For NGC 5548, upon the inclusion of a Gaussian line component in all the epochs, the value of the  $\chi^2$  reduced in the range 23–105, for a reduction of 2 d.o.f. Just an absorbed power law fit to the data produced a

reduced  $\chi^2$  of greater than 1.2 for epochs C, D, E, and F. Adding the Gaussian with the power law led to a reduced  $\chi^2$  of  $\sim 1.1$  for epochs C and D and  $\sim 1.0$  for epochs E and F. Similarly, for epochs A and B, the  $\chi^2$ /d.o.f. changed from 1.10 to 1.06 and 1.02 to 0.97, respectively. The width of the FeK $\alpha$  line was frozen to the value of 0.1 keV during the fitting, and leaving it free to vary did not improve the fit significantly. The best-fit parameters for the sources are given in Tables 2–4 for NGC 3227, MR 2251–178, and NGC 5548.

### 3.1.2. Pexrav

In the residuals of the simple power law fit to all the spectra of the sources (see Fig. 1), we found the signature of a high energy turnover and a reflection hump beyond 15 keV. To appropriately model both the high energy cutoff and the reflection feature present in the spectra, we replaced the  $zpo$  component in our earlier model with  $pexrav$ ; the new model has the form

$$const*TBabs(pexrav). \quad (3)$$

While modelling the reflection component of NGC 5548, the epoch G, H, and I spectra of NGC 3227, and the epoch E spectrum of MR 2251–178, an intrinsic absorption component,  $zTBabs$ , was added with the above model. The intrinsic hydrogen column density,  $N_{\text{H}}(zTBabs)$ , was kept free during the fit.

This model implements both photoelectric absorption and Compton scattering; however, it does not include fluorescence. Therefore, to model the FeK $\alpha$  line seen in the residual spectra in NGC 3227, NGC 5548, and epoch D in MR 2251–178, we included a Gaussian component. So, the model takes the form

$$const*TBabs(pexrav + zgauss). \quad (4)$$

in XSPEC. The model  $pexrav$  improved the fitting compared to  $zpo$ , as evidenced by the reduced  $\chi^2$  in Tables 2–4. This model

**Table 2.** Results of the fit to the spectra of NGC 3227.

| Parameter  | Epoch A                | Epoch B                | Epoch C                | Epoch D                | Epoch E                | Epoch F                | Epoch G                | Epoch H                | Epoch I                 |
|--|------------------------|------------------------|------------------------|------------------------|------------------------|------------------------|------------------------|------------------------|-------------------------|
| <b>Model I : <math>const*TBabs*zTBabs(zpo + zgauss)</math></b>     |                        |                        |                        |                        |                        |                        |                        |                        |                         |
| $\Gamma$   | $1.56^{+0.01}_{-0.01}$ | $1.55^{+0.01}_{-0.01}$ | $1.61^{+0.01}_{-0.01}$ | $1.63^{+0.01}_{-0.01}$ | $1.66^{+0.01}_{-0.01}$ | $1.63^{+0.01}_{-0.01}$ | $1.61^{+0.02}_{-0.02}$ | $1.64^{+0.04}_{-0.04}$ | $1.48^{+0.07}_{-0.07}$  |
| $N_H(zTBabs)$  | —                      | —                      | —                      | —                      | —                      | —                      | $2.91^{+1.04}_{-1.03}$ | $4.66^{+1.83}_{-1.80}$ | $4.57^{+3.73}_{-3.62}$  |
| $E$  | $6.35^{+0.03}_{-0.03}$ | $6.38^{+0.03}_{-0.04}$ | $6.33^{+0.04}_{-0.04}$ | $6.32^{+0.04}_{-0.03}$ | $6.30^{+0.05}_{-0.05}$ | $6.34^{+0.05}_{-0.05}$ | $6.23^{+0.04}_{-0.04}$ | $6.28^{+0.07}_{-0.07}$ | $6.38^{+0.05}_{-0.05}$  |
| EW   | $149^{+23}_{-32}$      | $188^{+32}_{-42}$      | $142^{+30}_{-35}$      | $129^{+22}_{-24}$      | $86^{+26}_{-30}$       | $115^{+26}_{-38}$      | $115^{+23}_{-23}$      | $123^{+44}_{-40}$      | $269^{+66}_{-81}$       |
| Norm   | $71^{+2}_{-2}$         | $58^{+2}_{-2}$         | $73^{+2}_{-2}$         | $90^{+3}_{-3}$         | $101^{+3}_{-3}$        | $92^{+3}_{-3}$         | $122^{+7}_{-6}$        | $76^{+8}_{-7}$         | $17^{+4}_{-3}$          |
| $\chi^2/d.o.f.$  | 930/826                | 752/706                | 834/704                | 909/777                | 815/790                | 684/717                | 1081/935               | 600/595                | 257/247                 |
| $C_{FPMA/FPMB}$  | $1.04^{+0.01}_{-0.01}$ | $1.02^{+0.01}_{-0.01}$ | $1.01^{+0.01}_{-0.01}$ | $1.01^{+0.01}_{-0.01}$ | $1.02^{+0.01}_{-0.01}$ | $1.00^{+0.01}_{-0.01}$ | $0.99^{+0.01}_{-0.01}$ | $1.04^{+0.01}_{-0.01}$ | $1.06^{+0.03}_{-0.03}$  |
| <b>Model II : <math>const*TBabs*zTBabs(pexrav + zgauss)</math></b> |                        |                        |                        |                        |                        |                        |                        |                        |                         |
| $\Gamma$   | $1.68^{+0.05}_{-0.05}$ | $1.64^{+0.06}_{-0.05}$ | $1.77^{+0.05}_{-0.05}$ | $1.83^{+0.04}_{-0.04}$ | $1.88^{+0.05}_{-0.05}$ | $1.82^{+0.05}_{-0.05}$ | $1.92^{+0.01}_{-0.07}$ | $1.85^{+0.08}_{-0.08}$ | $1.70^{+0.04}_{-0.11}$  |
| $N_H(zTBabs)$  | —                      | —                      | —                      | —                      | —                      | —                      | $6.43^{+0.92}_{-1.42}$ | $7.71^{+1.93}_{-1.95}$ | $8.52^{+4.30}_{-5.18}$  |
| $E_{cut}$  | $212^{+140}_{-63}$     | $163^{+118}_{-50}$     | >254                   | >1147                  | >411                   | >406                   | >571                   | >775                   | >126                    |
| $R$  | $0.52^{+0.15}_{-0.13}$ | $0.48^{+0.18}_{-0.15}$ | $0.53^{+0.18}_{-0.15}$ | $0.55^{+0.16}_{-0.14}$ | $0.73^{+0.19}_{-0.17}$ | $0.55^{+0.18}_{-0.16}$ | $0.83^{+0.16}_{-0.15}$ | $0.45^{+0.20}_{-0.18}$ | $0.38^{+0.49}_{-0.34}$  |
| $E$  | $6.35^{+0.03}_{-0.03}$ | $6.38^{+0.04}_{-0.04}$ | $6.33^{+0.04}_{-0.04}$ | $6.32^{+0.04}_{-0.04}$ | $6.31^{+0.06}_{-0.06}$ | $6.34^{+0.05}_{-0.05}$ | $6.23^{+0.04}_{-0.04}$ | $6.28^{+0.07}_{-0.07}$ | $6.38^{+0.06}_{-0.06}$  |
| EW   | $137^{+32}_{-20}$      | $177^{+37}_{-42}$      | $129^{+26}_{-33}$      | $116^{+25}_{-23}$      | $74^{+26}_{-21}$       | $102^{+32}_{-22}$      | $85^{+23}_{-19}$       | $102^{+34}_{-31}$      | $231^{+82}_{-74}$       |
| Norm   | $84^{+6}_{-6}$         | $66^{+6}_{-6}$         | $91^{+8}_{-7}$         | $119^{+8}_{-7}$        | $139^{+10}_{-10}$      | $120^{+9}_{-9}$        | $207^{+19}_{-25}$      | $112^{+18}_{-16}$      | $25^{+9}_{-9}$          |
| $\chi^2/d.o.f.$  | 856/824                | 711/704                | 784/702                | 831/775                | 714/788                | 625/715                | 920/933                | 577/593                | 253/245                 |
| $C_{FPMA/FPMB}$  | $1.04^{+0.01}_{-0.01}$ | $1.02^{+0.01}_{-0.01}$ | $1.01^{+0.01}_{-0.01}$ | $1.01^{+0.01}_{-0.01}$ | $1.02^{+0.01}_{-0.01}$ | $1.00^{+0.01}_{-0.01}$ | $0.99^{+0.01}_{-0.01}$ | $1.04^{+0.01}_{-0.01}$ | $1.06^{+0.03}_{-0.03}$  |
| <b>Model III : <math>const*TBabs*zTBabs(xillver)</math></b>        |                        |                        |                        |                        |                        |                        |                        |                        |                         |
| $\Gamma$   | $1.69^{+0.01}_{-0.01}$ | $1.69^{+0.01}_{-0.01}$ | $1.77^{+0.02}_{-0.01}$ | $1.83^{+0.01}_{-0.01}$ | $1.80^{+0.01}_{-0.01}$ | $1.79^{+0.01}_{-0.01}$ | $1.77^{+0.01}_{-0.01}$ | $1.87^{+0.02}_{-0.02}$ | $1.91^{+0.03}_{-0.03}$  |
| $N_H(zTBabs)$  | —                      | —                      | —                      | —                      | —                      | —                      | $4.73^{+0.57}_{-0.56}$ | $8.58^{+0.98}_{-1.08}$ | $12.12^{+1.86}_{-1.82}$ |
| $E_{cut}$  | $127^{+14}_{-12}$      | $92^{+10}_{-8}$        | $204^{+46}_{-34}$      | >439                   | $378^{+152}_{-91}$     | $326^{+123}_{-78}$     | $248^{+67}_{-34}$      | >510                   | >198                    |
| $R$  | $0.86^{+0.12}_{-0.12}$ | $1.09^{+0.17}_{-0.16}$ | $0.85^{+0.14}_{-0.13}$ | $0.76^{+0.14}_{-0.12}$ | $0.61^{+0.12}_{-0.09}$ | $0.71^{+0.14}_{-0.11}$ | $0.68^{+0.08}_{-0.08}$ | $0.64^{+0.16}_{-0.14}$ | $1.36^{+0.47}_{-0.40}$  |
| Norm   | $1.98^{+0.02}_{-0.03}$ | $1.46^{+0.02}_{-0.05}$ | $2.01^{+0.03}_{-0.03}$ | $2.98^{+0.04}_{-0.04}$ | $2.97^{+0.03}_{-0.03}$ | $2.75^{+0.04}_{-0.04}$ | $3.73^{+0.04}_{-0.04}$ | $2.72^{+0.03}_{-0.04}$ | $0.68^{+0.03}_{-0.03}$  |
| $\chi^2/d.o.f.$  | 868/826                | 728/706                | 785/704                | 837/777                | 735/790                | 627/717                | 976/935                | 579/595                | 260/247                 |
| $C_{FPMA/FPMB}$  | $1.04^{+0.01}_{-0.01}$ | $1.02^{+0.01}_{-0.01}$ | $1.01^{+0.01}_{-0.01}$ | $1.01^{+0.01}_{-0.01}$ | $1.02^{+0.01}_{-0.01}$ | $1.00^{+0.01}_{-0.01}$ | $0.99^{+0.01}_{-0.01}$ | $1.04^{+0.01}_{-0.01}$ | $1.06^{+0.03}_{-0.03}$  |
| <b>Model IV : <math>const*TBabs*zTBabs(xillverCP)</math></b>       |                        |                        |                        |                        |                        |                        |                        |                        |                         |
| $\Gamma$   | $1.78^{+0.01}_{-0.01}$ | $1.80^{+0.01}_{-0.01}$ | $1.83^{+0.01}_{-0.01}$ | $1.84^{+0.01}_{-0.01}$ | $1.83^{+0.01}_{-0.01}$ | $1.83^{+0.01}_{-0.01}$ | $1.82^{+0.01}_{-0.01}$ | $1.87^{+0.02}_{-0.02}$ | $1.91^{+0.04}_{-0.03}$  |
| $N_H(zTBabs)$  | —                      | —                      | —                      | —                      | —                      | —                      | $4.97^{+0.59}_{-0.55}$ | $8.17^{+0.99}_{-0.82}$ | $12.21^{+1.73}_{-1.65}$ |
| $kT_e$   | $33^{+9}_{-7}$         | $28^{+9}_{-6}$         | $56^{+131}_{-18}$      | >80                    | >45                    | >47                    | $50^{+39}_{-10}$       | >85                    | >36                     |
| $R$  | $0.79^{+0.11}_{-0.11}$ | $0.96^{+0.18}_{-0.10}$ | $0.83^{+0.15}_{-0.15}$ | $0.78^{+0.13}_{-0.12}$ | $0.62^{+0.11}_{-0.11}$ | $0.71^{+0.14}_{-0.13}$ | $0.67^{+0.09}_{-0.10}$ | $0.65^{+0.16}_{-0.15}$ | $1.28^{+0.60}_{-0.30}$  |
| Norm   | $1.94^{+0.02}_{-0.02}$ | $1.52^{+0.02}_{-0.02}$ | $1.89^{+0.03}_{-0.03}$ | $2.56^{+0.02}_{-0.03}$ | $2.55^{+0.03}_{-0.05}$ | $2.50^{+0.04}_{-0.04}$ | $3.32^{+0.03}_{-0.07}$ | $2.24^{+0.07}_{-0.05}$ | $0.66^{+0.02}_{-0.02}$  |
| $\chi^2/d.o.f.$  | 881/826                | 746/706                | 790/704                | 838/777                | 733/790                | 629/717                | 970/935                | 581/595                | 261/247                 |
| $C_{FPMA/FPMB}$  | $1.04^{+0.01}_{-0.01}$ | $1.02^{+0.01}_{-0.01}$ | $1.01^{+0.01}_{-0.01}$ | $1.01^{+0.01}_{-0.01}$ | $1.02^{+0.01}_{-0.01}$ | $1.00^{+0.01}_{-0.01}$ | $0.99^{+0.01}_{-0.01}$ | $1.04^{+0.01}_{-0.01}$ | $1.06^{+0.03}_{-0.03}$  |
| Flux   | $1.04^{+0.02}_{-0.01}$ | $0.86^{+0.01}_{-0.01}$ | $0.94^{+0.01}_{-0.02}$ | $1.11^{+0.01}_{-0.01}$ | $1.15^{+0.01}_{-0.02}$ | $1.13^{+0.01}_{-0.01}$ | $1.55^{+0.01}_{-0.01}$ | $0.88^{+0.01}_{-0.01}$ | $0.27^{+0.01}_{-0.01}$  |

**Notes.** Models are Model I:  $const*TBabs*zTBabs(zpo + zgauss)$ , Model II:  $const*TBabs*zTBabs(pexrav + zgauss)$ , Model III:  $const*TBabs*zTBabs(xillver)$ , and Model IV:  $const*TBabs*zTBabs(xillverCP)$ . The  $zTBabs$  component is added with all the models to fit the epoch G, H, and I spectra. The fluxes are in units of  $10^{-10}$  erg  $cm^{-2}$   $s^{-1}$  in the 4–60 keV band except in epoch I, where the flux was calculated in the 4–50 keV band. The energy ( $E$ ) of the FeK $\alpha$  line, the equivalent width (EW) of the line,  $E_{cut}$ , and  $kT_e$  are expressed in units of keV, model normalization is in units of  $10^{-4}$  photons keV $^{-1}$   $cm^{-2}$   $s^{-1}$ , and  $N_H(zTBabs)$  is the host galaxy hydrogen column density in units of  $10^{22}$  atoms  $cm^{-2}$ .  $C_{FPMA/FPMB}$  is the cross-calibration constant. The width of the FeK $\alpha$  line was fixed to 0.1 keV during the fitting.

includes primary emission that has a power law form with an exponential cutoff and a reflection component. The reflector is considered to be an optically thick medium in an infinite plane geometry that covers a larger fraction of the X-ray source. A parameter that comes as an output in the model fit is the reflection parameter,  $R$ . This parameter gives a measure of the reflection component present in the observed spectra of the sources. For an isotropic source, this parameter is related to the solid angle ( $\Omega$ ) as  $R \sim \Omega/2\pi$ , and it is dependent on the angle of inclination ( $i$ ) between the perpendicular to the accretion disk and the line of sight to the observer. The width of the FeK $\alpha$  line was

fixed at 0.1 keV, and leaving the parameter free did not improve the fit. For all the sources, the parameters that were left free in the model fits are  $E_{cut}$ ,  $\Gamma$ ,  $R$ , and normalization.

Using ( $pexrav+zgauss$ ) in all nine epochs of NGC 3227, the  $\chi^2$  was reduced in the range between 4 and 161 for a reduction of 2 d.o.f. compared to the ( $zpo+zgauss$ ) fit. In MR 2251–178, the reduction in  $\chi^2$  is in the range between 0 and 22, with a reduction of 2 d.o.f. For all six epochs in NGC 5548, the ( $pexrav+zgauss$ ) fit produced a reduction in the  $\chi^2$  values between 9–60, with a reduction of 2 d.o.f. compared to ( $zpo+zgauss$ ). The best-fit parameters are given in Tables 2–4.

**Table 3.** Results of the model fits to the spectra of MR 2251–178.

| Parameter   | Epoch A                | Epoch B                | Epoch C                | Epoch D                | Epoch E                |
|---|------------------------|------------------------|------------------------|------------------------|------------------------|
| <b>Model I : <math>const*TBabs*zTBabs(zpo+zgauss)</math></b>      |                        |                        |                        |                        |                        |
| $\Gamma$  | $1.75^{+0.02}_{-0.02}$ | $1.79^{+0.01}_{-0.01}$ | $1.79^{+0.02}_{-0.02}$ | $1.79^{+0.02}_{-0.02}$ | $1.83^{+0.05}_{-0.05}$ |
| $N_H(zTBabs)$   | –                      | –                      | –                      | –                      | $7.82^{+2.99}_{-2.93}$ |
| $E$   | –                      | –                      | –                      | $6.49^{+0.37}_{-0.27}$ | –                      |
| EW  | <35                    | <49                    | <34                    | <70                    | <46                    |
| Norm  | $142^{+5}_{-5}$        | $177^{+6}_{-6}$        | $162^{+6}_{-6}$        | $162^{+6}_{-6}$        | $84^{+13}_{-11}$       |
| $\chi^2/d.o.f.$   | 583/601                | 656/633                | 574/551                | 516/576                | 446/400                |
| $C_{FPMA/FPMB}$   | $1.02^{+0.02}_{-0.02}$ | $1.00^{+0.01}_{-0.01}$ | $1.03^{+0.02}_{-0.02}$ | $1.02^{+0.02}_{-0.02}$ | $1.05^{+0.02}_{-0.02}$ |
| <b>Model II : <math>const*TBabs*zTBabs(pextrav+zgauss)</math></b> |                        |                        |                        |                        |                        |
| $\Gamma$  | $1.65^{+0.05}_{-0.05}$ | $1.72^{+0.05}_{-0.03}$ | $1.76^{+0.07}_{-0.07}$ | $1.79^{+0.06}_{-0.06}$ | $1.82^{+0.11}_{-0.10}$ |
| $N_H(zTBabs)$   | –                      | –                      | –                      | –                      | $7.66^{+3.26}_{-3.02}$ |
| $E_{cut}$   | $125^{+96}_{-39}$      | $185^{+200}_{-69}$     | $110^{+70}_{-32}$      | $193^{+417}_{-80}$     | >175                   |
| $R$   | <0.07                  | <0.11                  | $0.29^{+0.22}_{-0.18}$ | $0.19^{+0.20}_{-0.17}$ | <0.23                  |
| $E$   | –                      | –                      | –                      | $6.48^{+0.67}_{-0.31}$ | –                      |
| EW  | <49                    | <43                    | <33                    | <63                    | <50                    |
| Norm  | $111^{+8}_{-8}$        | $144^{+11}_{-6}$       | $139^{+15}_{-13}$      | $144^{+15}_{-13}$      | $75^{+19}_{-14}$       |
| $\chi^2/d.o.f.$   | 569/599                | 647/631                | 552/549                | 509/574                | 446/398                |
| $C_{FPMA/FPMB}$   | $1.02^{+0.02}_{-0.02}$ | $1.00^{+0.01}_{-0.01}$ | $1.03^{+0.02}_{-0.02}$ | $1.02^{+0.02}_{-0.02}$ | $1.05^{+0.02}_{-0.02}$ |
| <b>Model III : <math>const*TBabs*zTBabs(xillver)</math></b>       |                        |                        |                        |                        |                        |
| $\Gamma$  | $1.65^{+0.02}_{-0.02}$ | $1.72^{+0.02}_{-0.02}$ | $1.70^{+0.02}_{-0.02}$ | $1.77^{+0.02}_{-0.02}$ | $1.82^{+0.02}_{-0.03}$ |
| $N_H(zTBabs)$   | –                      | –                      | –                      | –                      | $7.56^{+1.69}_{-1.38}$ |
| $E_{cut}$   | $124^{+22}_{-18}$      | $169^{+45}_{-30}$      | $103^{+18}_{-14}$      | $163^{+46}_{-30}$      | >366                   |
| $R$   | <0.10                  | <0.16                  | $0.17^{+0.14}_{-0.13}$ | $0.22^{+0.15}_{-0.13}$ | <0.11                  |
| Norm  | $2.92^{+0.02}_{-0.04}$ | $3.54^{+0.03}_{-0.05}$ | $2.79^{+0.05}_{-0.05}$ | $3.05^{+0.02}_{-0.05}$ | $2.10^{+0.03}_{-0.52}$ |
| $\chi^2/d.o.f.$   | 569/599                | 647/631                | 556/549                | 510/576                | 447/398                |
| $C_{FPMA/FPMB}$   | $1.02^{+0.02}_{-0.02}$ | $1.00^{+0.01}_{-0.01}$ | $1.03^{+0.02}_{-0.02}$ | $1.02^{+0.02}_{-0.02}$ | $1.05^{+0.02}_{-0.02}$ |
| <b>Model IV : <math>const*TBabs*zTBabs(xillverCP)</math></b>      |                        |                        |                        |                        |                        |
| $\Gamma$  | $1.76^{+0.01}_{-0.01}$ | $1.79^{+0.01}_{-0.01}$ | $1.80^{+0.02}_{-0.01}$ | $1.83^{+0.02}_{-0.01}$ | $1.83^{+0.02}_{-0.02}$ |
| $N_H(zTBabs)$   | –                      | –                      | –                      | –                      | $7.54^{+1.42}_{-1.45}$ |
| $kT_e$  | $25^{+26}_{-6}$        | $35^{+149}_{-11}$      | $21^{+8}_{-4}$         | $35^{+67}_{-11}$       | >32                    |
| $R$   | <0.06                  | <0.11                  | <0.25                  | $0.17^{+0.14}_{-0.13}$ | <0.09                  |
| Norm  | $2.68^{+0.02}_{-0.03}$ | $3.26^{+0.03}_{-0.05}$ | $2.66^{+0.04}_{-0.04}$ | $2.85^{+0.04}_{-0.04}$ | $1.71^{+0.02}_{-0.04}$ |
| $\chi^2/d.o.f.$   | 576/599                | 650/631                | 555/549                | 511/576                | 447/398                |
| $C_{FPMA/FPMB}$   | $1.02^{+0.02}_{-0.02}$ | $1.00^{+0.01}_{-0.01}$ | $1.03^{+0.02}_{-0.02}$ | $1.02^{+0.02}_{-0.02}$ | $1.05^{+0.02}_{-0.02}$ |
| Flux  | $1.07^{+0.01}_{-0.01}$ | $1.22^{+0.01}_{-0.01}$ | $1.08^{+0.01}_{-0.01}$ | $1.09^{+0.01}_{-0.01}$ | $0.47^{+0.02}_{-0.01}$ |

**Notes.** Models are Model I:  $const*TBabs*zTBabs(zpo)$ , Model II:  $const*TBabs*zTBabs(pextrav)$ , Model III:  $const*TBabs*zTBabs(xillver)$ , and Model IV:  $const*TBabs*zTBabs(xillverCP)$ . The  $zTBabs$  component is added with all the models to fit the epoch E spectra. In epoch D, the width of the FeK $\alpha$  line was fixed to 0.1 keV. In the case where no line was detected, the upper limit on the equivalent width (EW) was calculated by fixing the line energy to 6.4 keV. The fluxes are in units of  $10^{-10}$  erg cm $^{-2}$  s $^{-1}$  in the 4–60 keV band except in epoch E, where the flux was calculated in the 4–50 keV band. Columns and parameters have the same meaning as given for Table 2.

### 3.2. Physical model fits

Accretion disk reflection features in the form of a narrow FeK $\alpha$  line was conspicuously present in the residuals of NGC 3227, NGC 5548, and epoch D spectra of MR 2251–178, and the line was modelled using a Gaussian component in *pextrav* model fits. For MR 2251–178 we have seen signatures of reflection (though weak) in a few epochs. This is evident from the best-fit values of the reflection fraction obtained using *pextrav* (see Table 3) and in the residuals of the *zpo* model fits (see Fig. 2, top panel). We therefore modelled the spectra of the sources with the self-consistent ionized reflection model *xillver* (García & Kallman 2010; García et al. 2013). The emergent reflected spectrum from the surface of the X-ray illuminated accretion disk is calculated in the model by solving the equa-

tions of radiative transfer, energy balance, and ionization equilibrium in a Compton thick plane parallel medium (García et al. 2013). The model fit to the spectra has the following form in XSPEC,

$$const*TBabs(xillver). \quad (5)$$

Here also, to account for the effect of intrinsic absorption,  $zTBabs$  was used for all epochs of NGC 5548, three epochs (G, H, and I) of NGC 3227, and epoch E of MR 2251–178. The intrinsic hydrogen column densities,  $N_H(zTBabs)$ , were kept as free parameters. In this model fit, the parameters describing the properties of the corona, such as  $\Gamma$ ,  $E_{cut}$ , and  $R$ , were made to vary, while the inclination angle was frozen to the value of  $50^\circ$  for NGC 3227,  $30^\circ$  for NGC 5548, and  $60^\circ$  for MR 2251–178.

**Table 4.** Results of the model fits to the spectra of NGC 5548.

| Parameter   | Epoch A                | Epoch B                | Epoch C                | Epoch D                | Epoch E                | Epoch F                |
|---|------------------------|------------------------|------------------------|------------------------|------------------------|------------------------|
| Model I : $const*TBabs*zTBabs(zpo + zgauss)$      |                        |                        |                        |                        |                        |                        |
| $\Gamma$  | $1.62^{+0.03}_{-0.03}$ | $1.60^{+0.03}_{-0.03}$ | $1.59^{+0.02}_{-0.02}$ | $1.64^{+0.02}_{-0.02}$ | $1.57^{+0.03}_{-0.02}$ | $1.57^{+0.03}_{-0.01}$ |
| $N_H(zTBabs)$                                     | $3.89^{+1.76}_{-1.73}$ | <3.21                  | $6.29^{+1.40}_{-1.32}$ | $2.70^{+1.28}_{-1.27}$ | $8.97^{+1.65}_{-1.63}$ | <1.28                  |
| $E$   | $6.37^{+0.09}_{-0.09}$ | $6.33^{+0.08}_{-0.08}$ | $6.32^{+0.04}_{-0.04}$ | $6.38^{+0.04}_{-0.04}$ | $6.66^{+0.04}_{-0.04}$ | $6.31^{+0.04}_{-0.04}$ |
| EW  | $70^{+42}_{-23}$       | $89^{+27}_{-31}$       | $117^{+34}_{-34}$      | $107^{+28}_{-29}$      | $114^{+26}_{-44}$      | $137^{+24}_{-45}$      |
| Norm  | $100^{+10}_{-9}$       | $86^{+11}_{-11}$       | $79^{+8}_{-8}$         | $93^{+7}_{-6}$         | $77^{+6}_{-5}$         | $67^{+5}_{-2}$         |
| $\chi^2/d.o.f.$                                   | 684/643                | 612/634                | 880/811                | 890/813                | 840/810                | 692/692                |
| $C_{FPMA/FPMB}$                                   | $1.02^{+0.02}_{-0.02}$ | $1.05^{+0.01}_{-0.01}$ | $1.02^{+0.01}_{-0.01}$ | $1.05^{+0.01}_{-0.01}$ | $1.02^{+0.01}_{-0.01}$ | $1.05^{+0.01}_{-0.01}$ |
| Model II : $const*TBabs*zTBabs(pextrav + zgauss)$ |                        |                        |                        |                        |                        |                        |
| $\Gamma$  | $1.75^{+0.02}_{-0.10}$ | $1.81^{+0.02}_{-0.08}$ | $1.62^{+0.10}_{-0.10}$ | $1.79^{+0.09}_{-0.09}$ | $1.61^{+0.10}_{-0.11}$ | $1.81^{+0.08}_{-0.09}$ |
| $N_H(zTBabs)$                                     | $6.06^{+1.58}_{-2.46}$ | $4.77^{+1.31}_{-2.05}$ | $5.61^{+2.34}_{-2.36}$ | $4.46^{+2.13}_{-2.16}$ | $6.91^{+2.45}_{-2.47}$ | $3.66^{+1.18}_{-2.10}$ |
| $E_{cut}$   | >345                   | >502                   | $152^{+158}_{-54}$     | >170                   | $160^{+178}_{-58}$     | >414                   |
| $R$   | $0.19^{+0.14}_{-0.11}$ | $0.35^{+0.16}_{-0.14}$ | $0.28^{+0.11}_{-0.10}$ | $0.37^{+0.12}_{-0.11}$ | $0.33^{+0.12}_{-0.10}$ | $0.42^{+0.14}_{-0.13}$ |
| $E$   | $6.37^{+0.10}_{-0.10}$ | $6.32^{+0.09}_{-0.10}$ | $6.32^{+0.04}_{-0.04}$ | $6.38^{+0.05}_{-0.05}$ | $6.35^{+0.04}_{-0.04}$ | $6.31^{+0.05}_{-0.05}$ |
| EW  | $55^{+38}_{-27}$       | $64^{+31}_{-46}$       | $114^{+24}_{-38}$      | $89^{+25}_{-20}$       | $113^{+29}_{-34}$      | $104^{+44}_{-27}$      |
| Norm  | $126^{+7}_{-23}$       | $125^{+15}_{-19}$      | $79^{+18}_{-15}$       | $118^{+23}_{-20}$      | $73^{+17}_{-14}$       | $103^{+3}_{-17}$       |
| $\chi^2/d.o.f.$                                   | 675/641                | 588/632                | 834/809                | 840/811                | 780/808                | 652/690                |
| $C_{FPMA/FPMB}$                                   | $1.02^{+0.02}_{-0.02}$ | $1.05^{+0.01}_{-0.01}$ | $1.02^{+0.01}_{-0.01}$ | $1.05^{+0.01}_{-0.01}$ | $1.02^{+0.01}_{-0.01}$ | $1.05^{+0.01}_{-0.01}$ |
| Model III : $const*TBabs*zTBabs(xillver)$         |                        |                        |                        |                        |                        |                        |
| $\Gamma$  | $1.75^{+0.02}_{-0.02}$ | $1.78^{+0.02}_{-0.04}$ | $1.68^{+0.02}_{-0.01}$ | $1.77^{+0.01}_{-0.01}$ | $1.66^{+0.01}_{-0.02}$ | $1.81^{+0.01}_{-0.01}$ |
| $N_H(zTBabs)$                                     | $6.47^{+0.98}_{-0.91}$ | $4.83^{+0.95}_{-0.91}$ | $7.13^{+0.73}_{-0.73}$ | $4.52^{+0.69}_{-0.67}$ | $8.16^{+0.76}_{-0.75}$ | $4.25^{+0.83}_{-0.81}$ |
| $E_{cut}$   | >487                   | >480                   | $129^{+15}_{-13}$      | $179^{+40}_{-23}$      | $133^{+15}_{-13}$      | >395                   |
| $R$   | $0.25^{+0.08}_{-0.08}$ | $0.36^{+0.10}_{-0.09}$ | $0.49^{+0.09}_{-0.08}$ | $0.49^{+0.08}_{-0.08}$ | $0.51^{+0.09}_{-0.08}$ | $0.54^{+0.11}_{-0.10}$ |
| Norm  | $4.35^{+0.10}_{-0.06}$ | $3.61^{+0.47}_{-0.14}$ | $2.20^{+0.03}_{-0.03}$ | $2.47^{+0.03}_{-0.03}$ | $2.07^{+0.04}_{-0.04}$ | $2.70^{+0.04}_{-0.04}$ |
| $\chi^2/d.o.f.$                                   | 677/643                | 595/634                | 851/811                | 849/813                | 792/810                | 666/692                |
| $C_{FPMA/FPMB}$                                   | $1.02^{+0.02}_{-0.02}$ | $1.05^{+0.01}_{-0.01}$ | $1.02^{+0.01}_{-0.01}$ | $1.05^{+0.01}_{-0.01}$ | $1.02^{+0.01}_{-0.01}$ | $1.05^{+0.01}_{-0.01}$ |
| Model IV : $const*TBabs*zTBabs(xillverCP)$        |                        |                        |                        |                        |                        |                        |
| $\Gamma$  | $1.77^{+0.02}_{-0.02}$ | $1.80^{+0.02}_{-0.03}$ | $1.79^{+0.01}_{-0.01}$ | $1.85^{+0.01}_{-0.01}$ | $1.77^{+0.01}_{-0.01}$ | $1.84^{+0.01}_{-0.02}$ |
| $N_H(zTBabs)$                                     | $6.47^{+0.99}_{-0.91}$ | $4.63^{+0.94}_{-0.92}$ | $8.72^{+0.73}_{-0.74}$ | $5.66^{+0.69}_{-0.68}$ | $9.79^{+0.76}_{-0.75}$ | $4.30^{+0.87}_{-0.92}$ |
| $kT_e$  | >53                    | >54                    | $39^{+14}_{-10}$       | $65^{+147}_{-24}$      | $38^{+12}_{-9}$        | >65                    |
| $R$   | $0.25^{+0.08}_{-0.09}$ | $0.35^{+0.11}_{-0.08}$ | $0.43^{+0.08}_{-0.08}$ | $0.46^{+0.09}_{-0.08}$ | $0.45^{+0.08}_{-0.08}$ | $0.55^{+0.11}_{-0.11}$ |
| Norm  | $3.46^{+0.05}_{-0.05}$ | $2.95^{+0.34}_{-0.04}$ | $2.23^{+0.03}_{-0.03}$ | $2.46^{+0.03}_{-0.04}$ | $2.07^{+0.03}_{-0.03}$ | $2.34^{+0.08}_{-0.03}$ |
| $\chi^2/d.o.f.$                                   | 677/643                | 595/634                | 855/811                | 852/813                | 795/810                | 667/692                |
| $C_{FPMA/FPMB}$                                   | $1.02^{+0.02}_{-0.02}$ | $1.05^{+0.01}_{-0.01}$ | $1.02^{+0.01}_{-0.01}$ | $1.05^{+0.01}_{-0.01}$ | $1.02^{+0.01}_{-0.01}$ | $1.05^{+0.01}_{-0.01}$ |
| Flux  | $1.23^{+0.01}_{-0.01}$ | $1.11^{+0.01}_{-0.01}$ | $1.02^{+0.01}_{-0.01}$ | $1.05^{+0.01}_{-0.01}$ | $0.96^{+0.01}_{-0.01}$ | $0.92^{+0.01}_{-0.01}$ |

**Notes.** Models are Model I:  $const*TBabs*zTBabs(zpo + zgauss)$ , Model II:  $const*TBabs*zTBabs(pextrav + zgauss)$ , Model III:  $const*TBabs*zTBabs(xillver)$ , and Model IV:  $const*TBabs*zTBabs(xillverCP)$ . The width of the FeK $\alpha$  line was frozen to the value of 0.1 keV during the fitting. The fluxes are in units of  $10^{-10}$  erg cm $^{-2}$  s $^{-1}$  in the 4–60 keV band except in epoch F, where the flux was derived in the 4–55 keV band. Columns and parameters have the same meaning as given for Table 2.

The other parameter that was kept free was the normalization. To account for a fair comparison between the  $E_{cut}$  values obtained from *pextrav* and *xillver*, the reflector was assumed to be neutral (i.e.  $\log \zeta = 0$  erg cm s $^{-1}$ ). Also treating the ionization as a free parameter returned results consistent with the ones obtained using  $\log \zeta = 0$  erg cm s $^{-1}$ . The value of the Fe abundance was fixed to the solar value. The results of the model fits are given in Tables 2–4. Fitting the spectra using *xillver* yielded values of  $E_{cut}$  similar to those obtained using *pextrav*, although the errors in the  $E_{cut}$  measurements using *xillver* are relatively small.

As we are interested in the determination of  $kT_e$  and its variation, we decided to use the thermal Comptonization model *xillverCP* (García et al. 2014). This model, which takes

the emission lines into account by assuming they originate from disk reflection, includes the Comptonization model *nthcomp* (Zdziarski et al. 1996; Życki et al. 1999) plus the ionized reflection model *xillver* (García & Kallman 2010; García et al. 2013). The model fit to the spectra has the following form in XSPEC:

$$const*TBabs(xillverCP). \quad (6)$$

We used *xillverCP* to model the primary continuum and the reflection spectrum simultaneously. Also, to address the intrinsic absorption present in the spectra of all epochs of NGC 5548, epochs G, H, and I of NGC 3227, and epoch E of MR 2251–178, the  $zTBabs$  component was added with the described model. The results of the model fits are given in Tables 2–4.

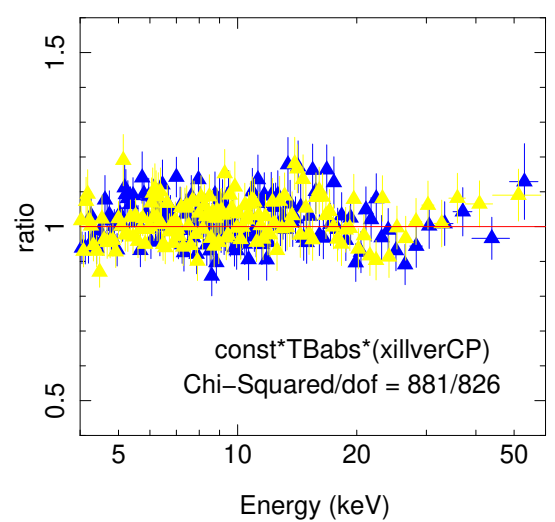
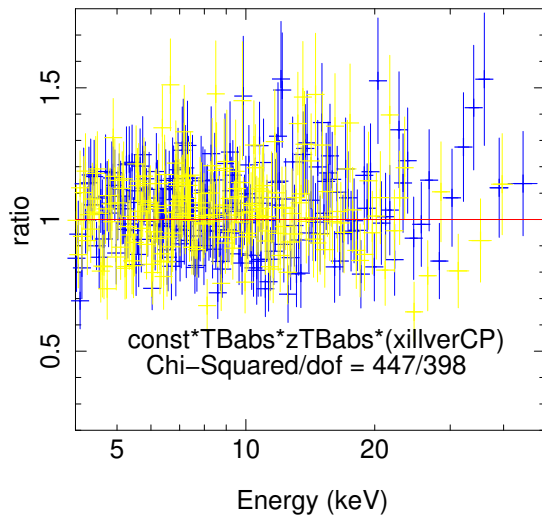
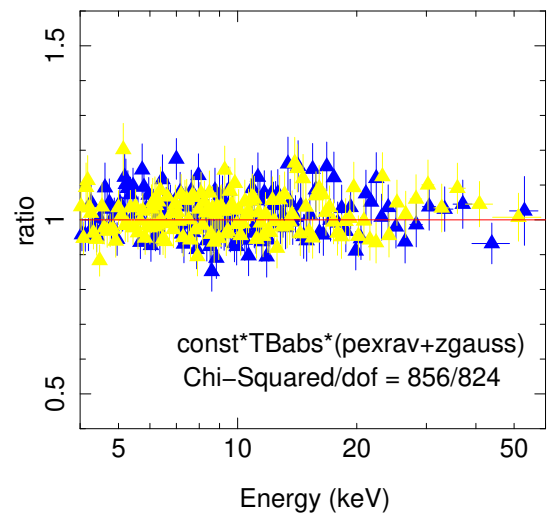
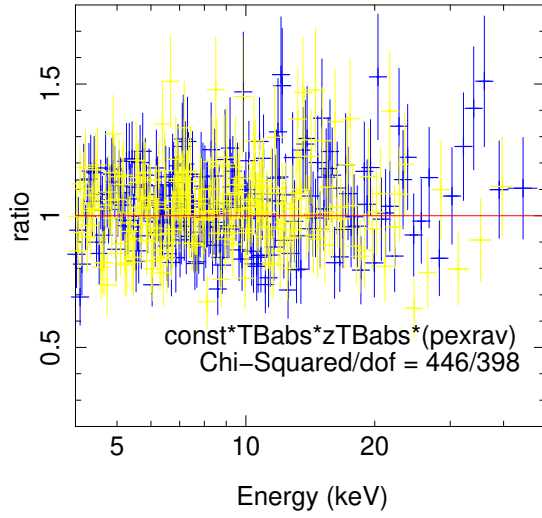
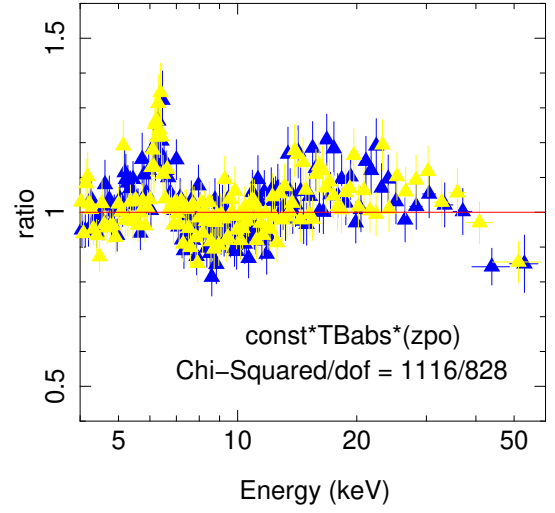
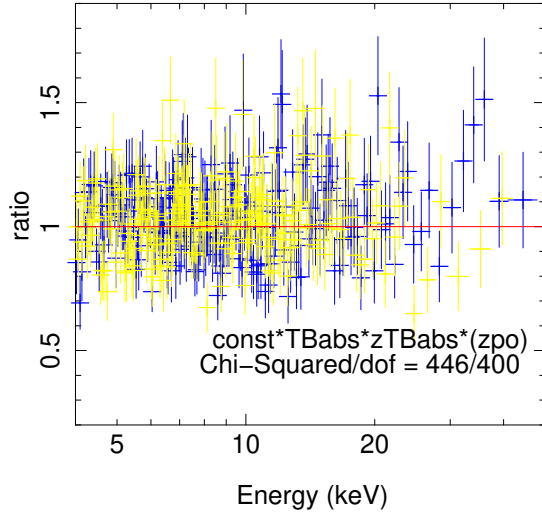


**Fig. 2.** Ratio of data to model for the model fits  $const*TBabs*zTBabs*(zpo)$ ,  $const*TBabs*zTBabs*(pexrav)$ , and  $const*TBabs*zTBabs*(xillverCP)$  to the FPMA (blue dot) and FPMB (yellow dot) spectra of ObsID 90601637002 of MR 2251–178. We re-binned the spectra for visualization purposes only.

**Fig. 3.** Ratio of data to the model for the model fits  $const*TBabs*(zpo + zgauss)$ ,  $const*TBabs*(pexrav + zgauss)$ , and  $const*TBabs*(xillverCP)$  to the FPMA (blue triangle) and FPMB (yellow triangle) spectra of ObsID 60202002002 of NGC 3227. The spectra are re-binned for visualization purposes.



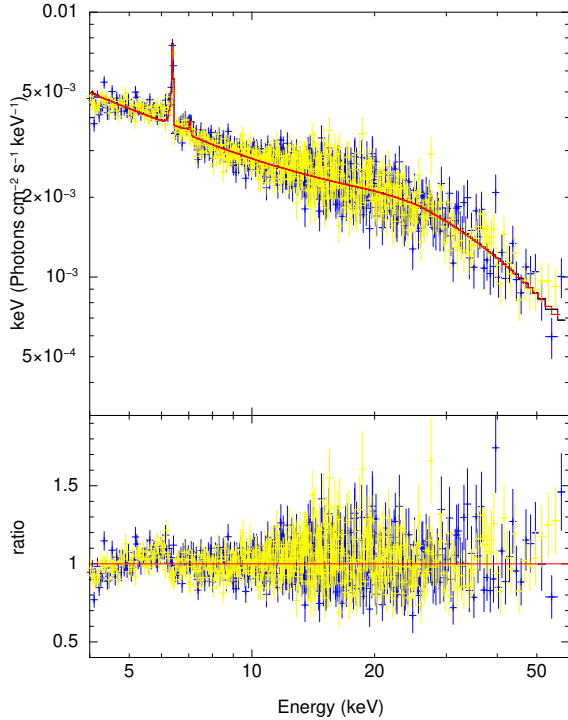


**Fig. 4.** Unfolded spectra with the data-to-model ratio for the model fits *const\*TBabs(xillverCP)* to the FPMA (blue) and FPMB (yellow) spectra of ObsID 60202002014 (epoch G) of NGC 3227.

## 4. Results and discussion

We aimed to find changes of  $kT_e$  in NGC 3227, NGC 5548, and MR 2251–178. We discuss below the results obtained for each.

### 4.1. NGC 3227

*NuSTAR* observed this source nine times between November 2016 and December 2019. Of these, results for seven epochs were reported by Kang et al. (2021), who were able to constrain  $E_{\text{cut}}$  in three epochs using phenomenological fits and  $kT_e$  in two epochs using physical model fits. Here, we report results for two additional epochs and for all nine epochs; we used both phenomenological and physical model fits to model the spectra.

Ratios of the model *const\*TBabs(zpo + zgauss)*, *const\*TBabs(pexrav + zgauss)*, and *const\*TBabs(xillverCP)* fits to the observed FPMA and FPMB spectra carried out on ObsID 60202002002, the one with the longest exposure time, are shown in Fig. 3. A weak FeK $\alpha$  line is present in all the ObsIDs, and therefore in the *const\*TBabs(zpo)* and *const\*TBabs(pexrav)* model fits we included a *zgauss* component to account for the line. All the above models could fit the spectra of all epochs of NGC 3227 reasonably well except for epochs G, H, and I, where the  $\chi^2/\text{d.o.f.}$  was greater than 1.2 and there is evidence for the presence of significant absorption at the low energy end (see Fig. 4). The addition of an extra absorption component – *zTBabs*, which takes the effects of host galaxy absorption into account – to all the models improved the fit significantly (see the left, middle, and right panel of Fig. 5). The *const\*TBabs(pexrav + zgauss)* model fit to the FPMA/FPMB spectra showed evidence for variation in  $E_{\text{cut}}$ . To analyse the variation in  $E_{\text{cut}}$  with time as well as to find the relation between  $E_{\text{cut}}$  and  $kT_e$ , we used the  $E_{\text{cut}}$  values obtained from *xillver* model fits. The

lowest value of  $E_{\text{cut}}$  of  $92^{+10}_{-8}$  keV was obtained in epoch B, the highest value of  $E_{\text{cut}}$  was observed in epoch E ( $378^{+152}_{-91}$  keV), and intermediate values of  $E_{\text{cut}}$  were obtained during other epochs. These observed variations in  $E_{\text{cut}}$  indicate that the coronal temperature of NGC 3227 must be changing with time. This is also evident in Fig. 6 (upper panel), where the values of  $E_{\text{cut}}$  are plotted against epochs. To quantify the significance of the variation in  $E_{\text{cut}}$ , we fitted a constant (the mean of all the  $E_{\text{cut}}$  measurements) to the variation in  $E_{\text{cut}}$  with epoch and calculated the  $\chi^2$  and the null hypothesis probability ( $p$ ) that  $E_{\text{cut}}$  does not change with time (shown as a dashed line in the top panel of Fig. 6). We found  $\chi^2/\text{d.o.f.} \gg 10$  and a  $p$  value of 0.0 that the  $E_{\text{cut}}$  does not change with time. The values of  $E_{\text{cut}}$  obtained during the first two epochs (A and B) are similar to the value of  $E_{\text{cut}} = 90 \pm 20$  keV reported by Markowitz et al. (2009). Vasudevan et al. (2013a), from an analysis of XMM and BAT spectra, estimated  $E_{\text{cut}}$  to lie outside the BAT range at  $>636$  keV. Recently, Kang et al. (2021) too reported  $E_{\text{cut}}$  values for epochs A, B, and G and lower limits for epochs C, D, E, and F from *pexrav* model fits. The values of  $E_{\text{cut}}$  obtained here using *xillver* for epochs A, B, and G are in agreement with those of Kang et al. (2021) from the *pexrav* model. Also, our model fits were able to constrain  $E_{\text{cut}}$  during epochs E and F using *xillver*.

Comptonization model fits using *xillverCP* provided values of  $kT_e$  that were also found to vary between epochs. We could constrain  $kT_e$  for epochs A, B, C, and G and obtain lower limits for epochs D, E, F, H, and I. Kang et al. (2021), using the same model used here, was only able to constrain  $kT_e$  for epochs A and B. Our results for epochs A and B are in agreement with those of Kang et al. (2021). The variation in  $kT_e$  is shown in the lower panel of Fig. 6. The trend seen in the variation in  $kT_e$  with epochs is similar to the variation in  $E_{\text{cut}}$ . From Comptonization model fits we found the lowest value of  $kT_e = 28^{+9}_{-6}$  keV during epoch B, while the highest value of  $kT_e = 56^{+131}_{-18}$  keV was obtained for epoch E. We obtained lower limits of  $kT_e$  of 80, 45, 47, 85, and 36 keV during epochs D, E, F, H, and I, respectively. Spectral fits using *xillverCP* along with the data-to-model ratio for all the epochs are shown in Figs. 5 and 7. The results of the model fits are given in Table 2. To quantify the significance of the variation in  $kT_e$ , we fitted a constant (the mean of all the  $kT_e$  measurements) to the variation in  $kT_e$  with epoch and calculated the  $\chi^2$  and the null hypothesis probability ( $p$ ) that  $kT_e$  does not change with time (shown as a dashed line in Fig. 6). We found a  $\chi^2/\text{d.o.f.}$  of 12.86 and a  $p$  value of 0.005 that  $kT_e$  does not change with time. The contour plots between  $\Gamma$  against  $kT_e$  and  $R$  against  $kT_e$  for NGC 3227 for all the epochs are shown in Figs. 8 and 9 (left panels). From the contour plots it is evident that the coronal temperature variation is prominent in NGC 3227. We therefore conclude that we found variation in the temperature of the corona in NGC 3227. According to Petrucci et al. (2001), for an optically thick corona ( $\tau > 1$ ),  $E_{\text{cut}} = 3kT_e$ . However, the relation between  $E_{\text{cut}}$  and  $kT_e$  can be complicated in the case of a non-static corona, such as the one with outflows (Liu et al. 2014). Also, according to Middei et al. (2019), the relation of  $E_{\text{cut}} = 2-3kT_e$  is valid only for low values of  $\tau$  and  $kT_e$ . For NGC 3227, using all five epochs in which we could constrain both  $E_{\text{cut}}$  and  $kT_e$ , we found  $E_{\text{cut}} = 3.94 \pm 0.62 kT_e$ , which is similar to that of Petrucci et al. (2001) and Middei et al. (2019).

### 4.2. MR 2251–178

This source has five epochs of observations that are public and have exposures  $>20$  ks. In this work we analysed all of them. Simple power law fits to the FPMA spectra of all the epochs

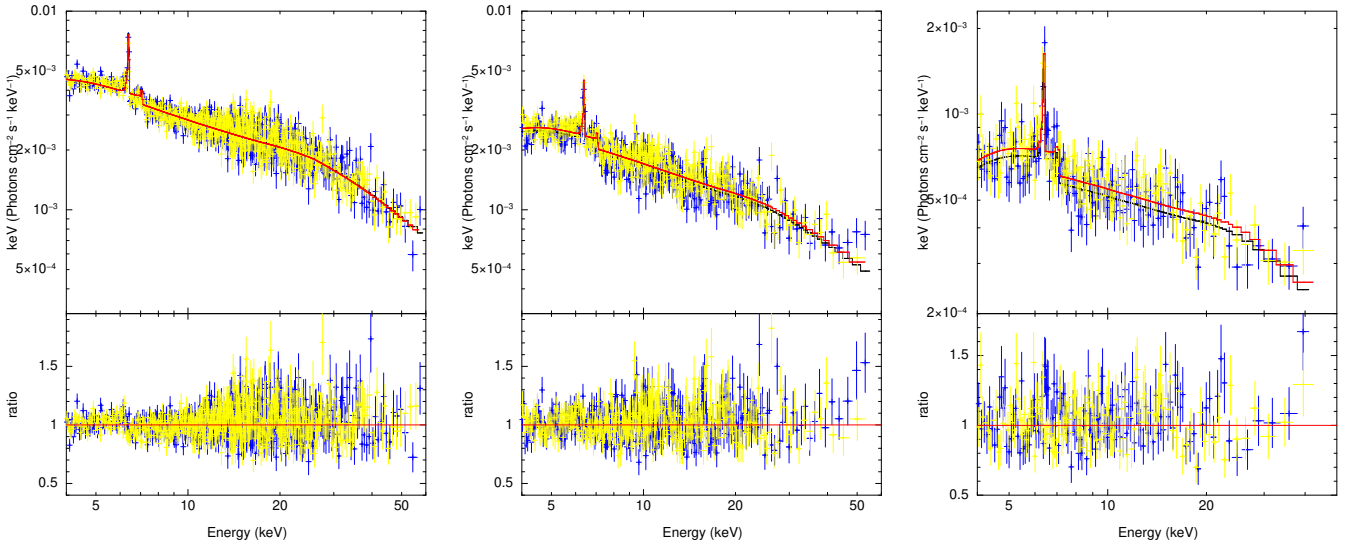


**Fig. 5.** Unfolded spectra and model fits along with the data-to-model ratio for *const\*TBabs(xillverCP)* fits to epoch G (left), epoch H (middle), and epoch I (right) of NGC 3227. For epochs G, H, and I, *zTBabs* was added to the model. Blue and yellow data points refer to FPMA and FPMB, respectively.

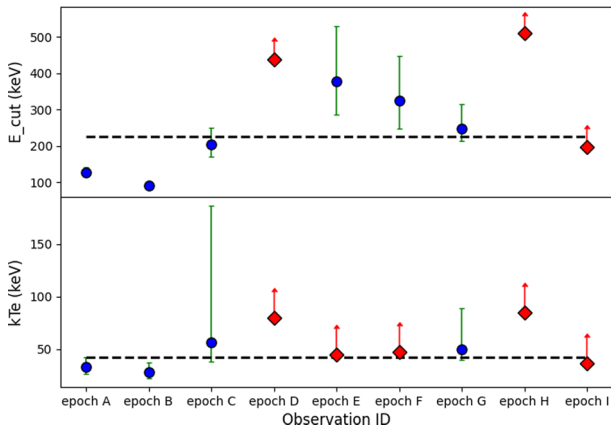


**Fig. 6.** Variation in  $E_{\text{cut}}$  and  $kT_e$  with the observation epochs as obtained from the *xillver* and *xillverCP* model fits, respectively, to the spectra of NGC 3227. The plotted errors were calculated using the  $\chi^2 = 2.71$  criterion, i.e. 90% confidence range. The dashed black lines in each panel are fits of constant (mean of  $E_{\text{cut}}$  and  $kT_e$ ) to the data points. For the fitting, epochs in which we were unable to constrain  $E_{\text{cut}}$  and  $kT_e$  were dropped (indicated with red diamonds).

are shown in the right panel of Fig. 1. From this figure, no noticeable change in the spectra could be ascertained. The ratio of the model fits *const\*TBabs(zpo)*, *const\*TBabs(pexrav)*, and *const\*TBabs(xillverCP)* to the observed FPMA and FPMB spectra on ObsID 90601637002, the one with the longest exposure time, are shown in Fig. 2. From two sets of observations from *Einstein* separated by about a year, Halpern (1984) found evidence of variable X-ray absorption in MR 2251–178, with the column density changing from  $<5 \times 10^{21} \text{ cm}^{-2}$  to  $2 \times 10^{22} \text{ cm}^{-2}$ ; this was suggested to be due to the presence of a warm absorber. *EXOSAT* and *Ginga* observations revealed a strong correspondence between the absorbing column density and the flux of the source, with the low energy absorption decreasing with the increasing flux of the source. These observations were explained by variable absorption in photo-ionized gas along the line of sight (Mineo & Stewart 1993; Pan et al. 1990). However, Walter & Courvoisier (1992), from an analysis of the *EXOSAT*

data, argued that the variability seen in the source can be explained without invoking the presence of a warm absorber. From the ratio of the observed data to the model fit, we did not find any signature of absorption that could affect the source spectra in all observations except epoch E, and to address this we added the *zTBabs* component to all four models in epoch E (see Figs. 10 and 11). Model fits to the four sets of observations that span about five years using *const\*TBabs(zpo)* do not reveal the presence of a FeK $\alpha$  line in the spectra, and the reflection bump was found to be either negligible or weak (see top panel of Fig. 2), likely due to poor S/N. However, the ratio plot for the model *const\*TBabs(zpo)* to the epoch D spectra revealed the presence of the FeK $\alpha$  line at around 6.4 keV. We therefore added a *zgauss* component with the model and found the energy of the line at  $6.49^{+0.37}_{-0.27}$  keV with a fixed width of 0.1 keV; leaving the parameter free did not significantly improve the fit. For this source the FeK $\alpha$  line has previously been reported to be present in the *Ginga* observations with an equivalent width of  $125^{+100}_{-105}$  eV (Mineo & Stewart 1993). Relatively strong FeK $\alpha$  was also reported to be present in the *BeppoSAX* observation (Orr et al. 2001), and a narrow FeK $\alpha$  line was present in the *Chandra* observations (Gibson et al. 2005). From *BeppoSAX* observations in the 0.1–200 keV band, Orr et al. (2001) found a  $E_{\text{cut}}$  value of around 100 keV, which is similar to that obtained here. To find evidence for the change in  $kT_e$ , if any, we carried out a fitting of the observations with the physical model, *const\*TBabs(xillverCP)*. An examination of the results of the fit (Table 3) shows that the  $kT_e$  obtained during all the epochs agree within errors. Though we could not find any signature of  $kT_e$  variation with epochs from the *xillverCP* fit, the  $E_{\text{cut}}$  values obtained from the *xillver* model fit during epochs A, C, and D agree within errors except that of epoch B. This could be due to the quality of the data in epoch B, as the values of  $E_{\text{cut}}$  and  $kT_e$  obtained during that epoch also have large error bars. To test for the  $kT_e$  variation, if any, we plotted the 90 per cent contours between  $kT_e$  and  $\Gamma$ . The 90 per cent contours of  $kT_e$  against  $\Gamma$  overlap (see Fig. 8), and we conclude that in MR 2251–178 we did not find any variation in  $kT_e$  with time. The 90 per cent contours of  $R$  against  $kT_e$  are also shown in the bottom panel of Fig. 9. Considering all four epochs where  $E_{\text{cut}}$  and  $kT_e$  could be

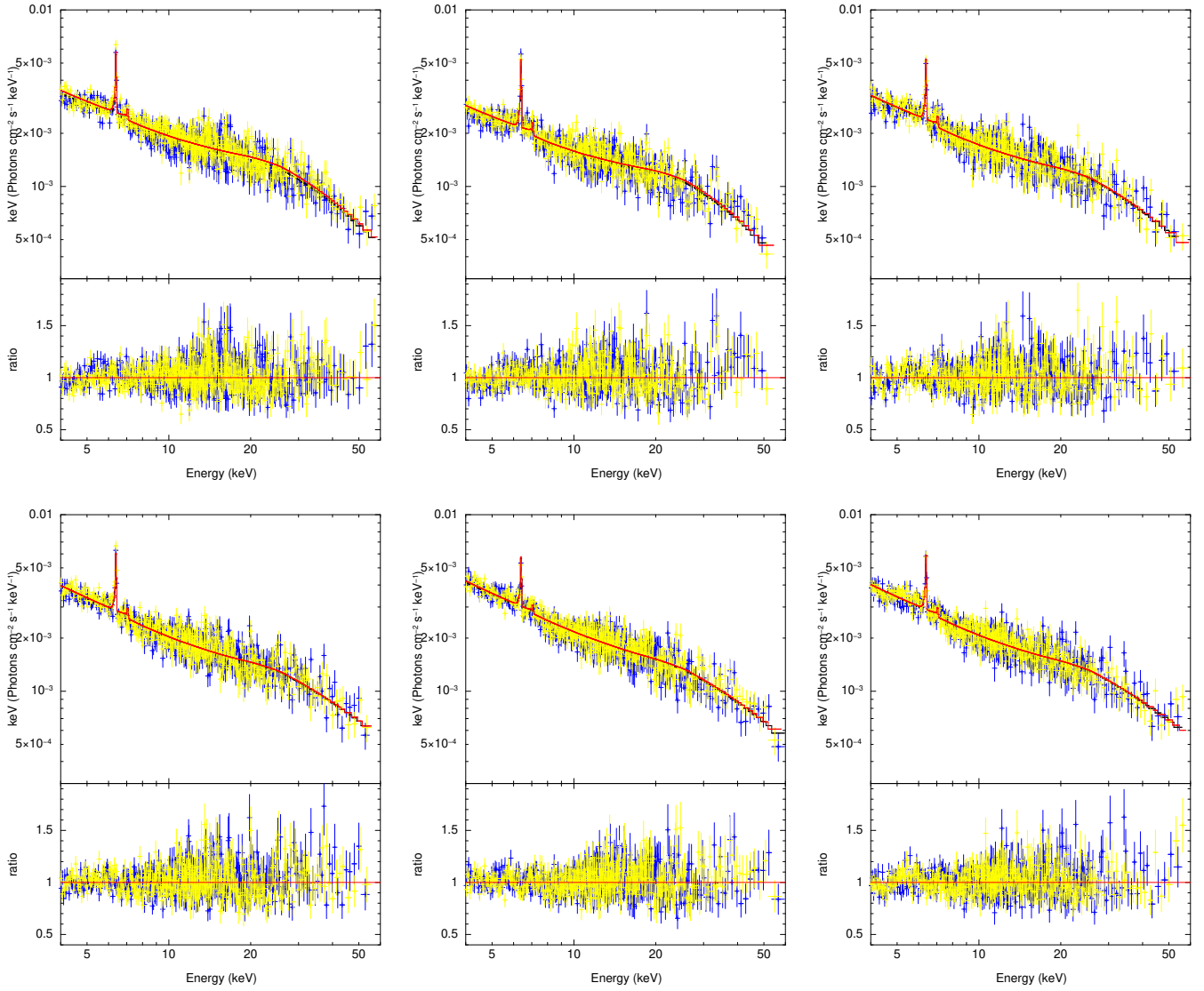


**Fig. 7.** Unfolded spectra along with *const\*TBabs(xillverCP)* model fits and the data-to-model ratio for epoch A (top-left panel), epoch B (top-middle panel), epoch C (top-right panel), epoch D (bottom-left panel), epoch E (bottom-middle panel), and epoch F (bottom-right panel) for the source NGC 3227. Blue and yellow data points refer to FPMA and FPMB, respectively.

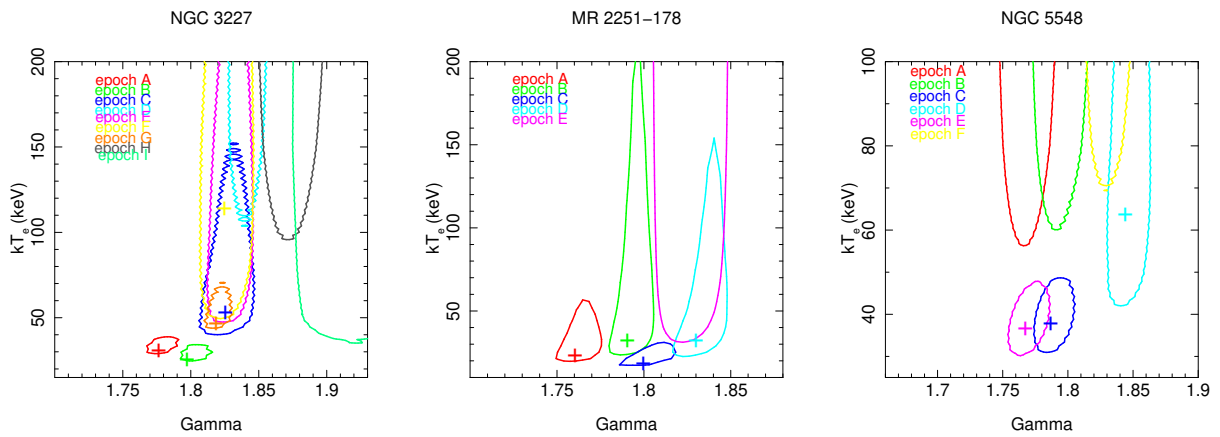


**Fig. 8.** 90 per cent confidence level contours between  $kT_e$  and  $\Gamma$  for the *xillverCP* model fit to the FPMA/FPMB spectra of NGC 3227 (left), MR 2251–178 (middle), and NGC 5548 (right). The colours indicate different ObsIDs. Here for MR 2251–178 the limits of  $kT_e$  do not have a correspondence with the values given in Table 3. This is because the contours were generated by freezing the  $R$  parameter so as to put all five ObsIDs together.

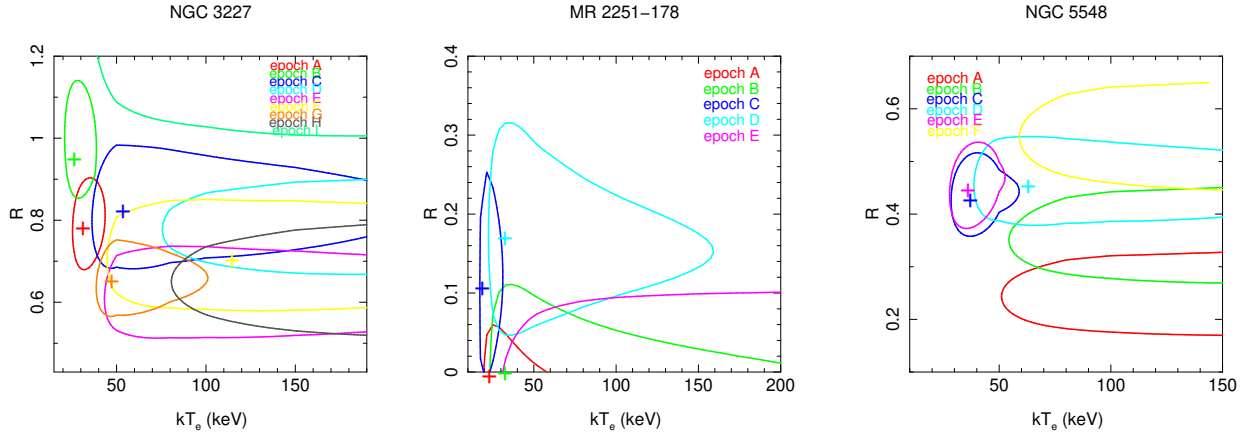


**Fig. 9.** 90 per cent confidence level contours between  $R$  and  $kT_e$  for the *xillverCP* model fit to the FPMA/FPMB spectra of NGC 3227 (left), MR 2251–178 (middle), and NGC 5548 (right).

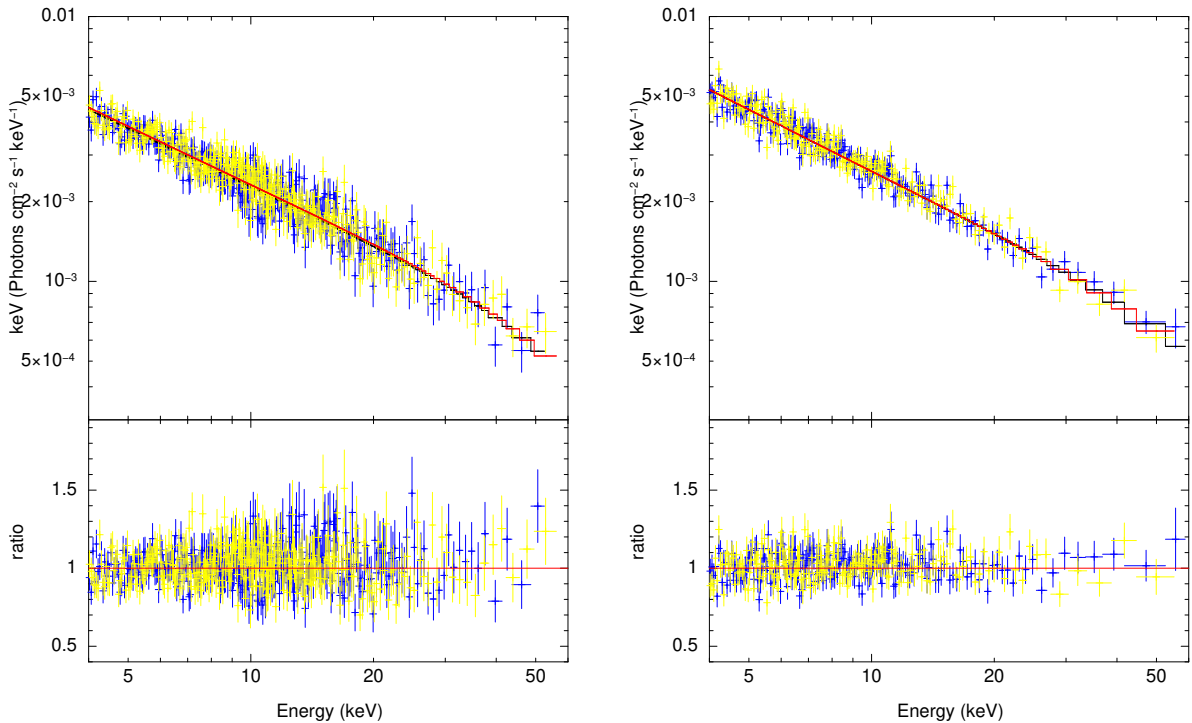


**Fig. 10.** Unfolded spectra along with the data-to-model ratio for *const\*TBabs(xillverCp)* fits to epoch A (left panel) and epoch B (right panel) observations of MR 2251–178. Here blue points are for FPMA and yellow points are for FPMB.

constrained, we found  $E_{\text{cut}} = 4.84 \pm 0.11 kT_e$ . This deviates from the generally adopted  $E_{\text{cut}} = 2-3kT_e$  (Petrucci et al. 2001). It is likely that the relation between  $E_{\text{cut}}$  and  $kT_e$  is complex and may depend on other physical properties of the sources. Homogeneous analyses of a large number of sources are needed to establish the relation between  $E_{\text{cut}}$  and  $kT_e$  as well as its dependence on other physical properties. Spectral fits using *xillverCP* along with the residuals for all the epochs are shown in Figs. 10 and 11.

#### 4.3. NGC 5548

NGC 5548 was observed by *NuSTAR* six times between July 2013 and January 2021. Of these, Zhang et al. (2018) have reported results for five epochs. In this work we carried out both phenomenological and physical model fits for all six epochs. We fitted the spectra using *const\*TBabs(zpo + zgauss)*

and *const\*TBabs(pexrav + zgauss)* to model the primary power law emission and the reflection component along with the FeK $\alpha$  line, with the width of the line frozen to the value of 0.1 keV. From the ratio of the observed data to the model fit using *TBabs*, we found the presence of an absorption component in the spectra. So, unlike for the other sources, for NGC 5548 we added an extra component, *zTBabs*, in each model to account for the absorption by the host galaxy. Moreover, as *xillver* self-consistently models the reflected spectrum and its associated FeK $\alpha$  line, we also fitted the spectra using *xillver*, and  $E_{\text{cut}}$  values obtained using the *xillver* model were used to find variation in  $E_{\text{cut}}$ . The  $E_{\text{cut}}$  obtained from *xillver* model fits are  $>487$  keV,  $>480$  keV,  $129^{+15}_{-13}$  keV,  $179^{+40}_{-23}$  keV,  $133^{+15}_{-13}$ , and  $>394$  keV for epochs A, B, C, D, E, and F, respectively. The residuals of the fit to the spectra for epoch D, which has the maximum exposure time, for various models are given in Fig. 12, and the results of



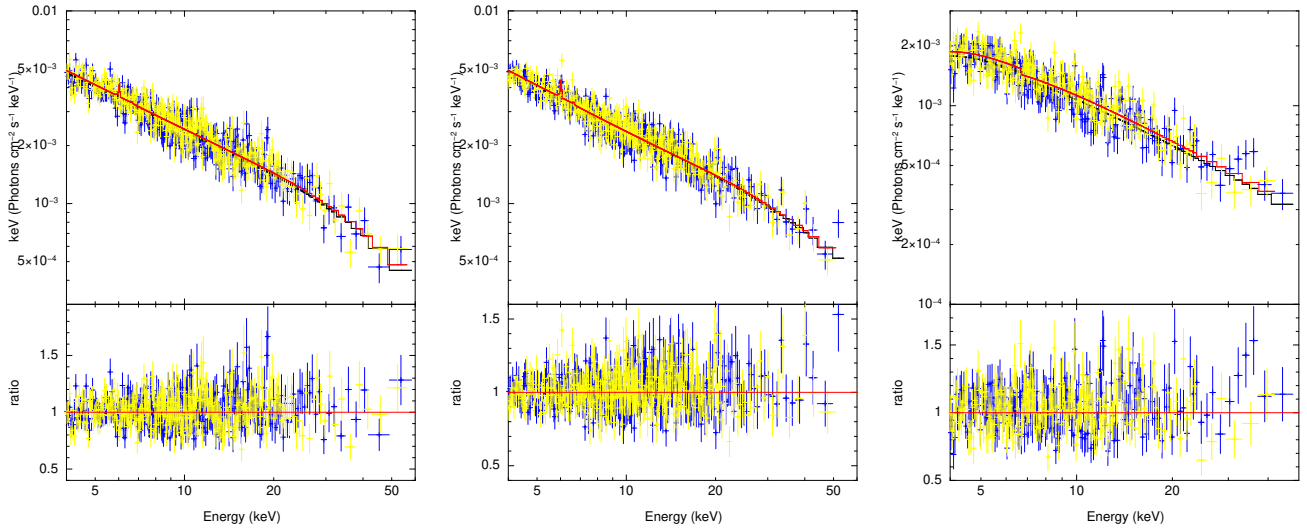


**Fig. 11.** Unfolded spectra along with the data-to-model ratio for *const\*TBabs(xillverCp)* fits to epoch C (left panel), epoch D (middle panel), and epoch E (right panel) observations of MR 2251–178. Here blue points are for FPMA and yellow points are for FPMB. In epoch E, the *zTBabs* component was added to the model.

the fit are given in Table 4. From *xillver* model fits, we could only constrain  $E_{\text{cut}}$  for epochs C, D, and E, while Zhang et al. (2018) could constrain  $E_{\text{cut}}$  in the four epochs (A, C, D, and E). For epochs C and D, our values of  $E_{\text{cut}}$  are in agreement with those of Zhang et al. (2018), but the results do not match for epoch E. Though Zhang et al. (2018) claims to have detected  $E_{\text{cut}}$  variation in NGC 5548, our analysis could not confirm changes in  $E_{\text{cut}}$ . This could be due to differences in the choice of binning and the energy ranges used in each work. Ursini et al. (2015), via the joint fitting of *XMM-Newton*, *Chandra*, *NuSTAR*, and *INTEGRAL* data, obtained lower limits for  $E_{\text{cut}}$  in all the epochs except for epoch D. Using the simultaneous *XMM-Newton* and *NuSTAR* data from the 2013 campaign, Cappi et al. (2016) also fitted the 4–79 keV epoch A and B together, epoch D, and epoch E spectra using a cutoff power law and *pexmon*. Their values of  $E_{\text{cut}}$  are in agreement with the  $E_{\text{cut}}$  values obtained in this work.

Fitting the physical Comptonization model *xillverCP* to ascertain the change in coronal temperature, we got the highest  $kT_e$  value of  $65^{+147}_{-24}$  keV during epoch D, for epochs A, B, and F we obtained lower limits of 53, 54, and 71 keV, and for the remaining two epochs, C and E, we obtained similar values of  $39^{+14}_{-10}$  keV and  $38^{+12}_{-9}$  keV, respectively. The values of  $kT_e$  between epochs agree with one another within error bars. The model fits to the data along with the data-to-model ratio for all the epochs of observation are shown in Figs. 13 and 14. The  $E_{\text{cut}}$  values obtained here point to variability. However, the derived  $kT_e$  values are consistent with one another within error bars. The contour plots between  $kT_e$  against  $\Gamma$  as well as  $R$  against  $kT_e$  are shown in the rightmost panels of Figs. 8 and 9. From these plots, the change in  $kT_e$  is not evident. We thus conclude that we have not found evidence for variation in  $kT_e$  in NGC 5548. Considering all the epochs in which we could constrain both  $E_{\text{cut}}$  and  $kT_e$ , we found  $E_{\text{cut}} = 3.19 \pm 0.32kT_e$ , which is in agreement with the empirical relation of Petrucci et al. (2001).

#### 4.4. Correlation between different parameters

We discuss below the correlation between various parameters. This is restricted to the source NGC 3227 as the temperature of its corona is found to vary in this work. Since the errors in the measured  $E_{\text{cut}}$  and  $kT_e$  values are not symmetric and there is

no conventional way to address such errors during a correlation study, we adopted two procedures to find the correlation between various parameters.

In the first case, we neglected the corresponding errors, considered only the best-fit values of the parameters, and performed the ordinary linear least square (OLS) fit between them. The Pearson’s correlation coefficient ( $r$ ) and the null hypothesis probability ( $p$ ) for no correlation were also estimated using the best-fit values.

In the second case, to take the non-symmetric errors into account, we simulated  $10^5$  points from each rectangular box around the best-fit values ( $x, y$ ) with  $x$  and  $y$  boundaries of ( $x_{\text{low}}, x_{\text{high}}$ ) and ( $y_{\text{low}}, y_{\text{high}}$ ), respectively. Here  $x_{\text{low}}, y_{\text{low}}$  and  $x_{\text{high}}, y_{\text{high}}$  refer to the lower and upper errors in  $x$  and  $y$  values. A linear least squares fit was done  $10^5$  times, yielding the distribution of the slope ( $m$ ), the intercept ( $c$ ), the Pearson’s rank correlation coefficient, and the probability of no correlation. The median values of the distributions were taken to represent the best-fit values of the correlation. All the values and the errors for the unweighted correlation as well as for the simulated correlation are given in Table 5.

##### 4.4.1. $\Gamma$ versus flux

In Seyfert galaxies, the X-ray spectra are generally found to be softer with increasing X-ray flux (Markowitz et al. 2003). We show in Fig. 15 the correlation between  $\Gamma$  and the brightness of NGC 3227. For the source, each point in the figure corresponds to the  $\Gamma$  and flux obtained by *xillverCP* model fits to each epoch of spectra. Shown are (a) the OLS fit to the data, (b) the linear least square fit employing the median values of the simulated points, using the lower and upper errors in  $\Gamma$  and flux values, and (c) the area bounded by the errors in the least square fit parameters. For NGC 3227, we found an anti-correlation between  $\Gamma$  and flux (see Fig. 15 and Table 5) between epochs of observation significant at the greater than 90 per cent level.

##### 4.4.2. $kT_e$ versus flux

Correlations between the changes in the temperature of the corona with other physical parameters of the sources, such as its apparent brightness and spectral shape, can provide important

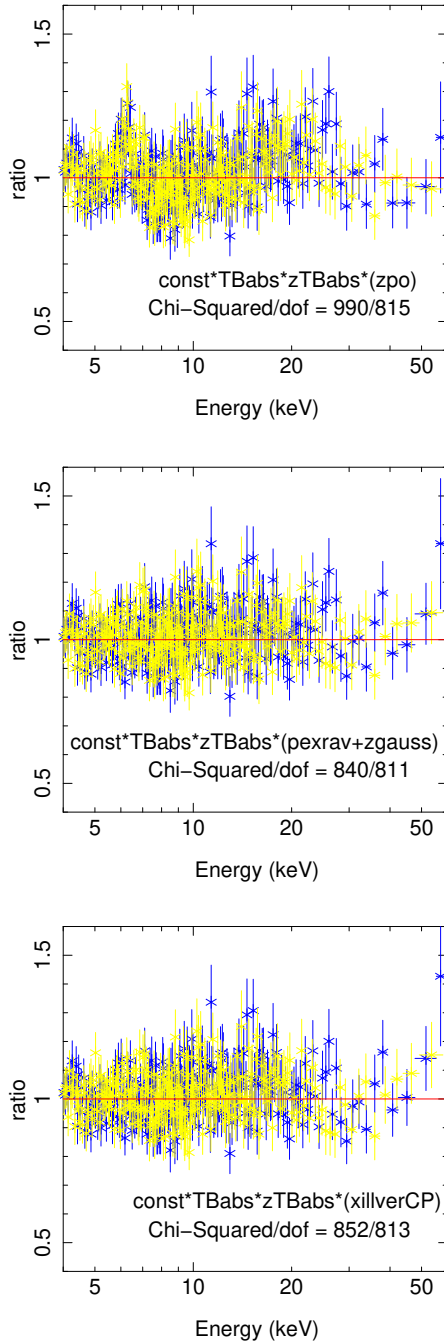


**Fig. 12.** Ratio plots for the model fits  $const*TBabs*zTBabs*(zpo + zgauss)$ ,  $const*TBabs*zTBabs*(pexrav + zgauss)$ , and  $const*TBabs*zTBabs*(xillverCP)$  to the FPMA (blue star) and FPMB (yellow star) spectra of ObsID 60002044006 of NGC 5548. The spectra are re-binned for visualization purposes only.

constraints and enhance our understanding of AGN corona. The correlation between  $kT_e$  and flux is shown in Fig. 15. Also shown in the figure are the ordinary and simulated linear least squares fits to the data. No correlation is found between  $kT_e$  and flux in NGC 3227.

#### 4.4.3. $\Gamma$ versus $kT_e$

In Fig. 16 the correlation between  $\Gamma$  and  $kT_e$  is shown, including the ordinary and simulated least square fits to the data. The correlation between  $\Gamma$  and  $kT_e$  is found to be not significant.

#### 4.4.4. $R$ versus $kT_e$

The correlation between the distant reflection fraction ( $R$ ) and  $kT_e$  is presented in the bottom panel of Fig. 16. We did not find any correlation between these two parameters.

#### 4.5. Nature of the corona in AGN

The primary X-ray emission from thermal Comptonization depends on the optical depth ( $\tau$ ) and  $kT_e$  as (Zdziarski et al. 1996; Życki et al. 1999)

$$\tau = \sqrt{\frac{9}{4} + \frac{3}{\theta \left[ \left( \Gamma + \frac{1}{2} \right)^2 - \frac{9}{4} \right]}} - \frac{3}{2}, \quad (7)$$

where  $\theta = kT_e/m_e c^2$ . We show in Fig. 17 the variation in the reflection fraction, the optical depth, and the Compton ‘y’ parameter with flux. The Compton y parameter is defined as (Petrucci et al. 2001)

$$y \simeq 4 \left( \frac{4kT_e}{mc^2} \right) \left[ 1 + \left( \frac{4kT_e}{mc^2} \right) \right] \tau (1 + \tau). \quad (8)$$

According to Stern et al. (1995), a Comptonized corona must have a constant y in equilibrium. We too found no correlation of y with the flux of the source. The parameter  $\tau$  is found not to show any statistically significant variation with flux, and  $R$  is not found to be correlated with flux either (see Fig. 17).

The few multiple epochs of observation of AGN available today point to  $E_{\text{cut}}$  increasing with the flux of the sources. For example, from an analysis of *NuSTAR* and *XMM-Newton* observations of NGC 5548, Zhang et al. (2018) found  $E_{\text{cut}}$  to be positively correlated with the flux of the source. Similarly, in Mrk 335, Keek & Ballantyne (2016), through a joint fitting of *Suzaku* and *NuSTAR*, found  $E_{\text{cut}}$  to be positively correlated with flux. Recently, from flux resolved spectroscopy of Ark 564, Barua et al. (2020) found the temperature of the corona to decrease with increasing flux. Also, for the source ESO 103–035 Barua et al. (2021) found a positive correlation between  $kT_e$  and flux. Scenarios that could cause the change in the temperature of the corona or  $E_{\text{cut}}$  in AGN are (a) Compton cooling and (b) an expanding corona. In the Compton cooling scenario, as the source brightens there will be an increase in seed UV photons from the disk for Comptonization, leading to a cooling of the corona. This leads to a ‘cooler when brighter behaviour’. In the expanding corona scenario, the increase in  $kT_e$  during high flux states of the AGN could be due to changes in the geometry of the corona. This has been invoked to explain the  $E_{\text{cut}}$  changes in Mrk 335 (Keek & Ballantyne 2016) and NGC 5548 (Zhang et al. 2018). According to the expanding corona model, at low flux state the corona is warm, optically thick, compact, and close to the black hole. This causes more illumination of the disk, leading to a larger reflection fraction. As the source increases in brightness, the corona expands, the optical depth drops, and the temperature rises. A reduced reflection fraction during this period implies that the corona expands vertically from the disk. In NGC 3227 too, the corona temperature is found to vary with time. We found a negative correlation between the optical depth ( $\tau$ ) and  $kT_e$ , with  $\tau$  decreasing towards higher temperatures (see Fig. 18). We calculated  $\tau$  using Eq. (7) and, according to Zdziarski et al. (1996),  $\tau$  is geometry dependent and equals the radial optical depth in a uniform sphere. The negative correlation between  $\tau$  and  $kT_e$  implies a change in the geometry of the corona (Ballantyne et al. 2014). Tortosa et al. (2018) too,

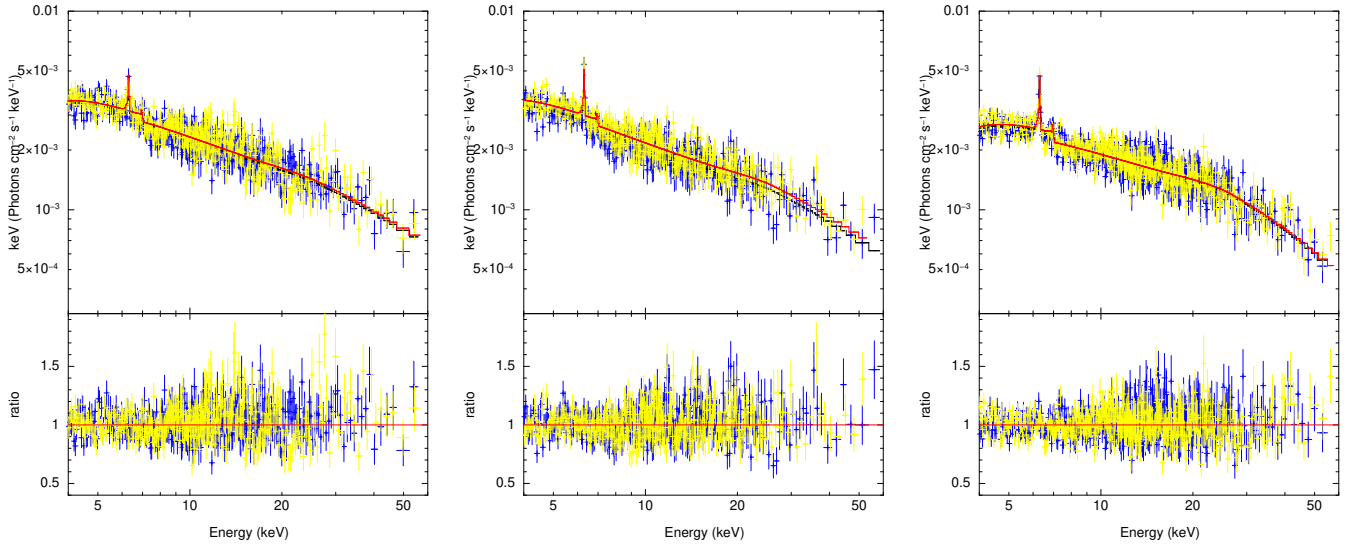


**Fig. 13.** Unfolded spectra with the data-to-model ratio and the  $const*TBabs*zTBabs(xillverCP)$  model fits to the spectra of NGC 5548. Here epoch A is shown in the *left panel*, epoch B is shown in the *middle panel*, and epoch C is shown in the *right panel*. Data from FPMA and FPMB are shown in blue and yellow, respectively.

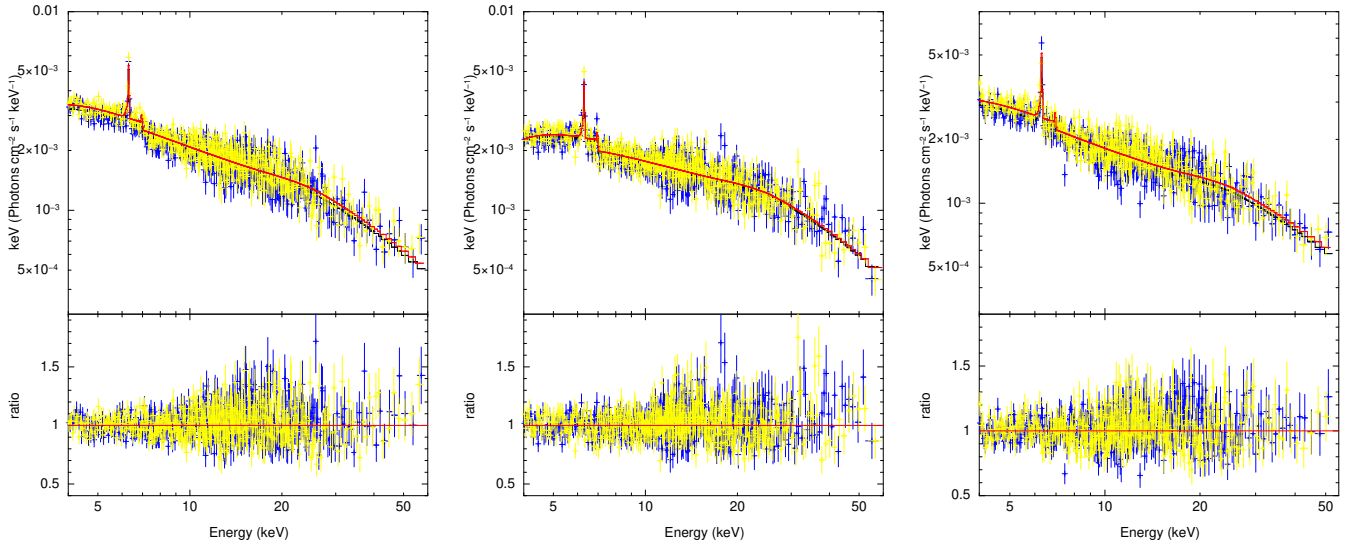


**Fig. 14.** Unfolded spectra with the data-to-model ratio and the  $const*TBabs*zTBabs(xillverCP)$  model fits to the spectra of NGC 5548. Here the *left, middle, and right panels* show the results for epochs D, E, and F, respectively. Data from FPMA and FPMB are shown in blue and yellow, respectively.

**Table 5.** Results of the correlation analysis between different parameters for NGC 3227.

| Parameter            | OLS                |                  |         |        | Simulated           |                  |         |        |
|----------------------|--------------------|------------------|---------|--------|---------------------|------------------|---------|--------|
|                      | $m$                | $c$              | $r$     | $p$    | $m$                 | $c$              | $r$     | $p$    |
| $\Gamma/\text{Flux}$ | $-0.07 \pm 0.03$   | $1.90 \pm 0.03$  | $-0.63$ | $0.07$ | $-0.07 \pm 0.03$    | $1.91 \pm 0.04$  | $-0.64$ | $0.06$ |
| $kT_e/\text{Flux}$   | $18 \pm 28$        | $22 \pm 31$      | $0.42$  | $0.58$ | $18 \pm 150$        | $13 \pm 169$     | $0.08$  | $0.52$ |
| $\Gamma/kT_e$        | $0.001 \pm 0.0006$ | $1.75 \pm 0.03$  | $0.86$  | $0.14$ | $0.0005 \pm 0.0002$ | $1.78 \pm 0.02$  | $0.80$  | $0.20$ |
| $R/kT_e$             | $-0.005 \pm 0.005$ | $1.03 \pm 0.22$  | $-0.57$ | $0.43$ | $-0.001 \pm 0.002$  | $0.90 \pm 0.17$  | $-0.36$ | $0.60$ |
| $R/\text{Flux}$      | $-0.51 \pm 0.13$   | $1.31 \pm 0.13$  | $-0.84$ | $0.01$ | $-0.04 \pm 0.15$    | $0.78 \pm 0.16$  | $-0.09$ | $0.68$ |
| $\tau/\text{Flux}$   | $-0.29 \pm 0.62$   | $2.35 \pm 0.65$  | $-0.17$ | $0.66$ | $-0.98 \pm 1.88$    | $3.15 \pm 2.12$  | $-0.35$ | $0.65$ |
| $y/\text{Flux}$      | $-0.15 \pm 0.70$   | $13.06 \pm 0.79$ | $-0.15$ | $0.85$ | $-0.53 \pm 1.50$    | $14.01 \pm 1.71$ | $-0.21$ | $0.66$ |
| $\tau/kT_e$          | $-0.043 \pm 0.002$ | $4.19 \pm 0.09$  | $-0.99$ | $0.00$ | $-0.02 \pm 0.00$    | $3.44 \pm 0.28$  | $-0.97$ | $0.03$ |

**Notes.** Provided are the slope ( $m$ ), intercept ( $c$ ), Pearson's correlation coefficient ( $r$ ), and the probability ( $p$ ) for null hypothesis (no correlation) from the OLS fit and the least squares fit from simulated points. See Sect. 4.4.

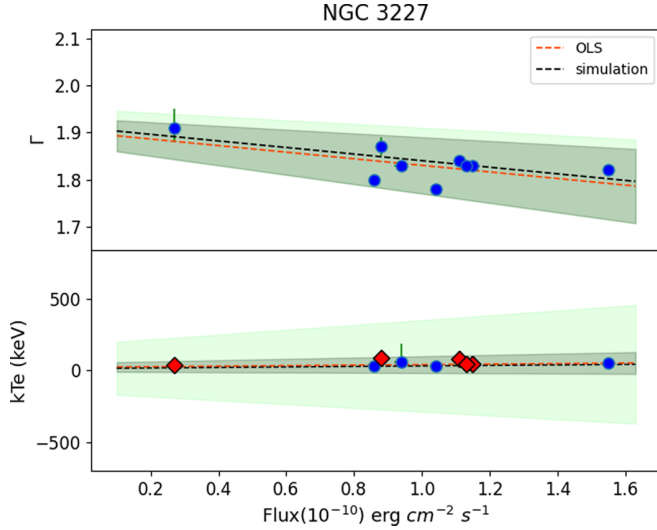


**Fig. 15.** Correlation of  $\Gamma$  and  $kT_e$  with the X-ray brightness of NGC 3227. The dashed orange line is the OLS fit to the data points. The dashed black line is the linear line drawn using the median values of the simulated parameters. The grey shaded region indicates the upper and lower errors in the fit parameters for OLS, and the green region indicates the errors in the fit parameter obtained from the simulation. In the least square analysis, epochs in which we were unable to constrain  $kT_e$  were dropped (indicated with red diamonds).

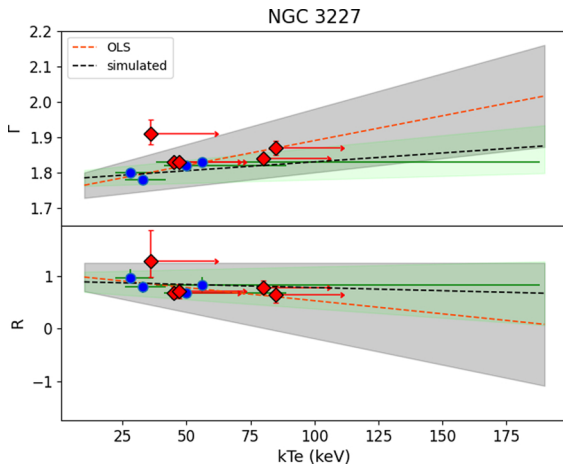


**Fig. 16.** Correlation between  $\Gamma$  and  $R$  with the  $kT_e$  of NGC 3227. The dashed lines and shaded regions have the same meaning as in Fig. 15. Epochs in which  $kT_e$  could not be constrained (shown as red diamonds) were not included in the linear least square analysis.

from the analysis of a sample of AGN, found a negative correlation between  $\tau$  and  $kT_e$ . According to the authors, this negative correlation could not be explained with a fixed disk-corona configuration in radiative balance. The possible explanation for this kind of behaviour could be (a) due to the change in the geometry and position of the corona and/or (b) variation in the fraction of the intrinsic disk emission to the total disk emission. We note that broadband spectral energy distribution fits to simultaneous UV to hard X-ray data alone will be able to provide a strong constraint on  $\tau$ . This in turn can put constraints on the role of accretion disk emission in  $kT_e$  changes. In NGC 3227 we found no statistically significant correlations between  $kT_e$  and flux, between  $R$  and flux, between  $\Gamma$  and flux, or between  $\Gamma$  and  $kT_e$ .

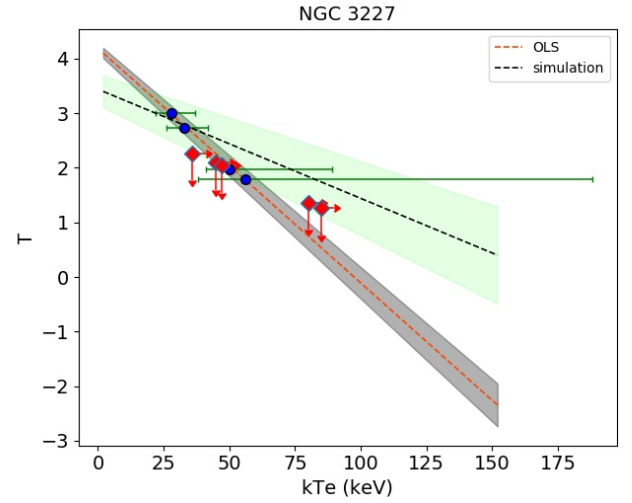


**Fig. 17.** Correlation between the  $\tau$  and  $kT_e$  of NGC 3227. The dashed lines and the shaded regions have the same meaning as in Fig. 15. The red diamonds shown were not considered for the linear least squares fit.

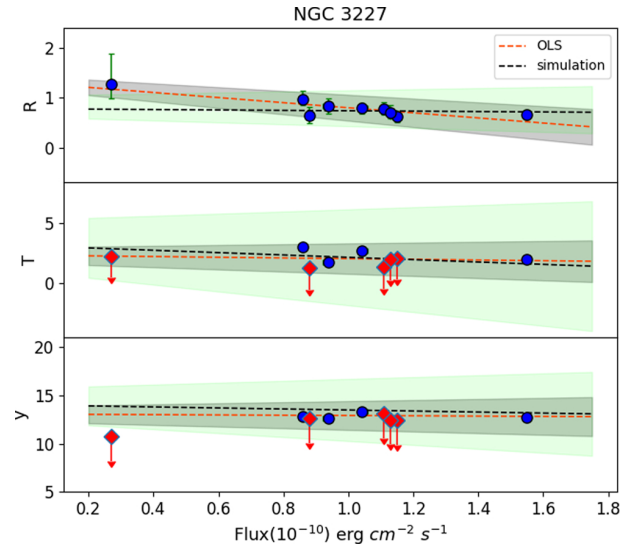


**Fig. 18.** Distant reflection fraction ( $R$ ), the optical depth ( $\tau$ ), and Compton- $y$  parameter as a function of flux for the source NGC 3227. The dashed lines and the shaded regions have the same meaning as in Fig. 15. The red diamonds were not included in the linear least squares fit.

## 5. Summary

In this work, we carried out spectral analyses of the *NuSTAR* data for three Seyfert-type AGN, namely NGC 3227, NGC 5548, and MR 2251–178, including a few ObsIDs that had not been analysed in previous works. We summarize our results below:

1. All the sources were found to show moderate variations in their average brightness during the epochs analysed in this work.
2. In NGC 3227, we found unambiguous evidence for the change in the temperature of the corona. This change in  $kT_e$  is also reflected in the variation in  $E_{\text{cut}}$ . For NGC 5548 and MR 2251–178 we found no evidence for variation in the temperature of the corona.

The variation in the temperature of the corona is known for fewer than half a dozen sources. Details on such a coronal temperature



variation in more AGN are needed to pinpoint the reasons for the corona temperature variation and its effect on the other physical properties of the sources.

**Acknowledgements.** We thank the anonymous referee for her/his useful comments and suggestions which improved the quality and the clarity of the paper. We thank the *NuSTAR* Operations, Software and Calibration teams for support with the execution and analysis of these observations. This research has made use of the *NuSTAR* Data Analysis Software (NuSTARDAS) jointly developed by the ASI Science Data Center (ASDC, Italy) and the California Institute of Technology (USA). This research has made use of data and/or software provided by the High Energy Astrophysics Science Archive Research Center (HEASARC), which is a service of the Astrophysics Science Division at NASA/GSFC.

## References

- Alonso-Herrero, A., García-Burillo, S., Pereira-Santaella, M., et al. 2019, *A&A*, **628**, A65
- Arnaud, K. A. 1996, in *XSPEC: The First Ten Years*, eds. G. H. Jacoby, & J. Barnes, *ASP Conf. Ser.*, **101**, 17
- Ballantyne, D. R. 2020, *MNRAS*, **491**, 3553
- Ballantyne, D. R., & Xiang, X. 2020, *MNRAS*, **496**, 4255
- Ballantyne, D. R., Bollenbacher, J. M., Brenneman, L. W., et al. 2014, *ApJ*, **794**, 62
- Baloković, M., Harrison, F. A., Madejski, G., et al. 2020, *ApJ*, **905**, 41
- Barua, S., Jithesh, V., Misra, R., et al. 2020, *MNRAS*, **492**, 3041
- Barua, S., Jithesh, V., Misra, R., et al. 2021, *ApJ*, **921**, 46
- Bentz, M. C., & Katz, S. 2015, *PASP*, **127**, 67
- Bergeron, J., Boksenberg, A., Dennefeld, M., & Tarengi, M. 1983, *MNRAS*, **202**, 125
- Bhayani, S., & Nandra, K. 2011, *MNRAS*, **416**, 629
- Bianchi, S., Guainazzi, M., Matt, G., Fonseca Bonilla, N., & Ponti, G. 2009, *A&A*, **495**, 421
- Cappi, M., De Marco, B., Ponti, G., et al. 2016, *A&A*, **592**, A27
- Chartas, G., Kochanek, C. S., Dai, X., Poindexter, S., & Garmire, G. 2009, *ApJ*, **693**, 174
- Crummy, J., Fabian, A. C., Gallo, L., & Ross, R. R. 2006, *MNRAS*, **365**, 1067
- Dadina, M. 2007, *A&A*, **461**, L209
- Della Ceca, R., Tagliaferri, G., Ghisellini, G., et al. 2010, *AAS/High Energy Astrophysics Division*, **11**, 7.08
- Dewangan, G. C., Mathur, S., Griffiths, R. E., & Rao, A. R. 2008, *ApJ*, **689**, 762
- Done, C., Davis, S. W., Jin, C., Blaes, O., & Ward, M. 2012, *MNRAS*, **420**, 1848
- Fabian, A. C. 1999, *Proc. Nat. Acad. Sci.*, **96**, 4749
- Fabian, A. C., Ballantyne, D. R., Merloni, A., et al. 2002, *MNRAS*, **331**, L35
- Fabian, A. C., Zoghbi, A., Ross, R. R., et al. 2009, *Nature*, **459**, 540
- Fabian, A. C., Lohfink, A., Belmont, R., Malzac, J., & Coppi, P. 2017, *MNRAS*, **467**, 2566
- García, J., & Kallman, T. R. 2010, *ApJ*, **718**, 695
- García, J., Dauser, T., Reynolds, C. S., et al. 2013, *ApJ*, **768**, 146
- García, J., Dauser, T., Lohfink, A., et al. 2014, *ApJ*, **782**, 76
- García, J., Kara, E., Walton, D., et al. 2019, *ApJ*, **871**, 88
- George, I. M., & Fabian, A. C. 1991, *MNRAS*, **249**, 352
- George, I. M., Mushotzky, R., Turner, T. J., et al. 1998, *ApJ*, **509**, 146
- Gibson, R. R., Marshall, H. L., Canizares, C. R., & Lee, J. C. 2005, *ApJ*, **627**, 83
- Gliozzi, M., & Williams, J. K. 2020, *MNRAS*, **491**, 532
- Haardt, F., & Maraschi, L. 1991, *ApJ*, **380**, L51
- Haardt, F., Maraschi, L., & Ghisellini, G. 1994, *ApJ*, **432**, L95
- Halpern, J. P. 1984, *ApJ*, **281**, 90
- Harrison, F. A., Craig, W. W., Christensen, F. E., et al. 2013, *ApJ*, **770**, 103
- Jin, C., Ward, M., Done, C., & Gelbord, J. 2012, *MNRAS*, **420**, 1825
- Johnson, W. N., McNaron-Brown, K., Kurfess, J. D., et al. 1997, *ApJ*, **482**, 173
- Kaastra, J. S., Kriss, G. A., Cappi, M., et al. 2014, *Science*, **345**, 64
- Kang, J.-L., Wang, J.-X., & Kang, W.-Y. 2021, *MNRAS*, **502**, 80
- Keek, L., & Ballantyne, D. R. 2016, *MNRAS*, **456**, 2722
- Komossa, S., & Fink, H. 1997, *A&A*, **327**, 483
- Lanzuisi, G., Gilli, R., Cappi, M., et al. 2019, *ApJ*, **875**, L20
- Liu, T., Wang, J.-X., Yang, H., Zhu, F.-F., & Zhou, Y.-Y. 2014, *ApJ*, **783**, 106
- Lobban, A. P., Turner, T. J., Reeves, J. N., Braitto, V., & Miller, L. 2020, *MNRAS*, **494**, 5056
- Lubiński, P., Zdziarski, A. A., Walter, R., et al. 2010, *MNRAS*, **408**, 1851
- Lubiński, P., Beckmann, V., Gibaud, L., et al. 2016, *MNRAS*, **458**, 2454
- Macchetto, F., Colina, L., Golombek, D., Perryman, M. A. C., & di Serego Alighieri, S. 1990, *ApJ*, **356**, 389
- Magdziarz, P., Blaes, O. M., Zdziarski, A. A., Johnson, W. N., & Smith, D. A. 1998, *MNRAS*, **301**, 179
- Malizia, A., Molina, M., Bassani, L., et al. 2014, *ApJ*, **782**, L25
- Markowitz, A., Edelson, R., Vaughan, S., et al. 2003, *ApJ*, **593**, 96
- Markowitz, A., Reeves, J. N., George, I. M., et al. 2009, *ApJ*, **691**, 922
- Matt, G., Fabian, A. C., & Ross, R. R. 1993, *MNRAS*, **262**, 179
- Matzeu, G. A., Nardini, E., Parker, M. L., et al. 2020, *MNRAS*, **497**, 2352
- McHardy, I. M., Gunn, K. F., Uttley, P., & Goad, M. R. 2005, *MNRAS*, **359**, 1469
- Mehdipour, M., Kaastra, J. S., Kriss, G. A., et al. 2015, *A&A*, **575**, A22
- Mehdipour, M., Kriss, G. A., Kaastra, J. S., et al. 2021, *A&A*, **652**, A150
- Middei, R., Bianchi, S., Marinucci, A., et al. 2019, *A&A*, **630**, A131
- Middei, R., Petrucci, P. O., Bianchi, S., et al. 2020, *A&A*, **640**, A99
- Middleton, M. J., Parker, M. L., Reynolds, C. S., Fabian, A. C., & Lohfink, A. M. 2016, *MNRAS*, **457**, 1568
- Mineo, T., & Stewart, G. C. 1993, *MNRAS*, **262**, 817
- Mushotzky, R. F., Done, C., & Pounds, K. A. 1993, *ARA&A*, **31**, 717
- Nandra, K., O'Neill, P. M., George, I. M., & Reeves, J. N. 2007, *MNRAS*, **382**, 194
- Netzer, H., Turner, T. J., & George, I. M. 1994, *ApJ*, **435**, 106
- Nicastro, F., Piro, L., De Rosa, A., et al. 2000, *ApJ*, **536**, 718
- Orr, A., Barr, P., Guainazzi, M., Parmar, A. N., & Young, A. J. 2001, *A&A*, **376**, 413
- Pan, H. C., Stewart, G. C., & Pounds, K. A. 1990, *MNRAS*, **242**, 177
- Petrucci, P. O., Haardt, F., Maraschi, L., et al. 2000, *ApJ*, **540**, 131
- Petrucci, P. O., Haardt, F., Maraschi, L., et al. 2001, *ApJ*, **556**, 716
- Petrucci, P. O., Paltani, S., Malzac, J., et al. 2013, *A&A*, **549**, A73
- Petrucci, P. O., Ursini, F., De Rosa, A., et al. 2018, *A&A*, **611**, A59
- Petrucci, P. O., Gronkiewicz, D., Rozanska, A., et al. 2020, *A&A*, **634**, A85
- Porquet, D., Reeves, J. N., Matt, G., et al. 2018, *A&A*, **609**, A42
- Rani, P., & Stalin, C. S. 2018a, *ApJ*, **856**, 120
- Rani, P., & Stalin, C. S. 2018b, *J. Astrophys. Astron.*, **39**, 15
- Rani, P., Stalin, C. S., & Goswami, K. D. 2019, *MNRAS*, **484**, 5113
- Rees, M. J. 1984, *ARA&A*, **22**, 471
- Reeves, J. N., Braitto, V., Porquet, D., et al. 2021, *MNRAS*, **500**, 1974
- Ricci, C., Walter, R., Courvoisier, T. J. L., & Paltani, S. 2011, *A&A*, **532**, A102
- Ricci, C., Trakhtenbrot, B., Koss, M. J., et al. 2017, *ApJS*, **233**, 17
- Ricker, G. R., Clarke, G. W., Doxsey, R. E., et al. 1978, *Nature*, **271**, 35
- Risaliti, G., Elvis, M., Fabbiano, G., Baldi, A., & Zezas, A. 2005, *ApJ*, **623**, L93
- Risaliti, G., Nardini, E., Salvati, M., et al. 2011, *MNRAS*, **410**, 1027
- Ross, R. R., & Fabian, A. C. 1993, *MNRAS*, **261**, 74
- Rózańska, A., Malzac, J., Belmont, R., Czerny, B., & Petrucci, P. O. 2015, *A&A*, **580**, A77
- Schmitt, H. R., Kinney, A. L., Storchi-Bergmann, T., & Antonucci, R. R. J. 1997, *ApJ*, **477**, 623
- Shakura, N. I., & Sunyaev, R. A. 1973, *A&A*, **500**, 33
- Stern, B. E., Poutanen, J., Svensson, R., Sikora, M., & Begelman, M. C. 1995, *ApJ*, **449**, L13
- Tazaki, F., Ueda, Y., Terashima, Y., & Mushotzky, R. F. 2011, *ApJ*, **738**, 70
- Tortosa, A., Bianchi, S., Marinucci, A., Matt, G., & Petrucci, P. O. 2018, *A&A*, **614**, A37
- Turner, T. J., Reeves, J. N., Braitto, V., et al. 2018, *MNRAS*, **481**, 2470
- Ursini, F., Boissay, R., Petrucci, P. O., et al. 2015, *A&A*, **577**, A38
- Ursini, F., Petrucci, P. O., Matt, G., et al. 2016, *MNRAS*, **463**, 382
- Vasudevan, R. V., Mushotzky, R. F., & Gandhi, P. 2013a, *ApJ*, **770**, L37
- Vasudevan, R. V., Brandt, W. N., Mushotzky, R. F., et al. 2013b, *ApJ*, **763**, 111
- Verner, D. A., Ferland, G. J., Korista, K. T., & Yakovlev, D. G. 1996, *ApJ*, **465**, 487
- Véron-Cetty, M. P., & Véron, P. 2010, *A&A*, **518**, A10
- Walter, R., & Courvoisier, T. J. L. 1992, *A&A*, **266**, 57
- Wang, J., Mao, Y. F., & Wei, J. Y. 2009, *AJ*, **137**, 3388
- Willingale, R., Starling, R. L. C., Beardmore, A. P., Tanvir, N. R., & O'Brien, P. T. 2013, *MNRAS*, **431**, 394
- Wilms, J., Allen, A., & McCray, R. 2000, *ApJ*, **542**, 914
- Xu, Y., García, J. A., Walton, D. J., et al. 2021, *ApJ*, **913**, 13
- Zdziarski, A. A., Johnson, W. N., & Magdziarz, P. 1996, *MNRAS*, **283**, 193
- Zdziarski, A. A., Poutanen, J., & Johnson, W. N. 2000, *ApJ*, **542**, 703
- Zhang, J.-X., Wang, J.-X., & Zhu, F.-F. 2018, *ApJ*, **863**, 71
- Zoghbi, A., Fabian, A. C., Reynolds, C. S., & Cackett, E. M. 2012, *MNRAS*, **422**, 129
- Zoghbi, A., Matt, G., Miller, J. M., et al. 2017, *ApJ*, **836**, 2
- Zycki, P. T., & Czerny, B. 1994, *MNRAS*, **266**, 653
- Zycki, P. T., Done, C., & Smith, D. A. 1999, *MNRAS*, **309**, 561